PHYSICAL REVIEW C **79**, 034310 (2009)

Variations on a theme by Skyrme: A systematic study of adjustments of model parameters

P. Klüpfel,[1] P.-G. Reinhard,[1] T. J. Bürvenich,[2] and J. A. Maruhn[3]
[1] *Institut für Theoretische Physik II, Universität Erlangen-Nürnberg, Staudtstrasse 7, D-91058 Erlangen, Germany*
[2] *Frankfurt Institute for Advanced Studies, Tuth-Moufang-Str. 1, D-60438 Frankfurt am Main, Germany*
[3] *Institut für Theoretische Physik, Universität Frankfurt, Max-von-Laue-Str. 1, D-60438 Frankfurt am Main, Germany*

(Received 21 April 2008; revised manuscript received 10 November 2008; published 13 March 2009)

We present a survey of the phenomenological adjustment of the parameters of the Skyrme-Hartree-Fock (SHF) model for a self-consistent description of nuclear structure and low-energy excitations. A large sample of reliable input data from nuclear bulk properties (energy, radii, surface thickness) is selected guided by the criterion that ground-state correlations should remain small. Least-squares fitting techniques are used to determine the SHF parameters that accommodate best the given input data. The question of the predictive value of the adjustment is scrutinized by performing systematic variations with respect to chosen nuclear matter properties (incompressibility, effective mass, symmetry energy, and sum-rule enhancement factor). We find that the ground-state data, although representing a large sample, leave a broad range of choices, i.e., a broad range of nuclear matter properties. Information from giant resonances is added to pin down more precisely the open features. We then apply the set of newly adjusted parametrizations to several more detailed observables such as neutron skin, isotope shifts, and super-heavy elements. The techniques of least-squares fitting provide safe estimates for the uncertainties of such extrapolations. The systematic variation of forces allows to disentangle the various influences on a given observable and to estimate the predictive value of the SHF model. The results depend very much on the observable under consideration.

DOI: 10.1103/PhysRevC.79.034310 PACS number(s): 21.10.Dr, 21.10.Ft, 21.10.Gv, 21.60.Jz

I. INTRODUCTION

The production of exotic nuclei far off the valley of stability is making steady progress at various laboratories around the world and is providing an increasing amount of new experimental data on basic nuclear properties (see, e.g., Refs. [1,2]). This is a great challenge for nuclear structure theory at all levels of refinement, from the more phenomenological microscopic-macroscopic methods (see, e.g., Ref. [3]) through self-consistent mean-field (SCMF) methods (see, e.g., Ref. [4]) or large shell-model calculations (see, e.g., Ref. [5]) up to several *ab initio* techniques employing a given nucleon-nucleon interaction (see, e.g., Refs. [6–8]). Further development of all these methods is a highly topical task for which a large network of activities has been launched recently [9]. The present article aims to contribute to the development of SCMF.

There are several approaches to SCMF from which the most widely used are the Skyrme-Hartree-Fock (SHF) model [4], the Gogny force [10], and the relativistic mean-field model (RMF) [11,12]. The genuine nucleon-nucleon interaction does not allow an immediate mean-field treatment. Thus all SCMF models employ effective interactions that are arranged to provide reliable nuclear structure properties and low-energy excitations at the level of a mean-field description. That approach has much in common with the density functional theory widely used in the physics of electronic systems [13]. The difference is, however, that electronic correlations are well under control and that reliable electronic energy-density functionals can be derived from well controlled *ab initio* calculations. The nuclear case is much more involved because the nucleon as such is a composite particle and a nucleon-nucleon interaction is already an approximate concept. Thus, nuclear many-body theories have not yet reached sufficient descriptive power to serve as direct input for deducing effective energy-density functionals for SCMF. Although there are promising attempts for an *ab initio* derivation [14], the general strategy for constructing energy functionals for high-quality calculations is to deduce the formal structure from principle considerations [15] and to rely on a phenomenological adjustment of the model parameters. The present article aims at a critical and thorough survey of the SHF model and the phenomenological adjustment of its parameters. There is a long history of SHF development and optimization (for recent reviews see Refs. [4,16]) and still the need for further intense consideration, as can be seen from the lively discussion in the literature, recent refitting attempts [17,18], and the huge combined effort in Ref. [9]. This study will point to several incompatibilities with the present SHF ansatz when trying to cover more than just the basic ground-state properties. We are thus not yet at the stage to advertise one preferred parametrization. The strategy is rather to supply a toolbox of forces produced under systematically varying conditions.

After a brief review of the basic SHF functional and the strategy of least-squares fitting, our considerations start with an inspection of the input data for the adjustment of the model parameters. The idea is to select those ground-state observables (energies, radii, surface thicknesses) that are expected to be well described by a pure mean-field model. The limits to a mean-field description are set by the ground-state correlations (GSC) stemming from low-lying collective quadrupole modes (for recent surveys, see Refs. [19–21]). Taking the general trends of GSC as worked out in Ref. [21], we determine a set of observables that have only small correlation effects and that we use as basis for the fits of mean-field models. We then will investigate in detail how predictive such fits can be. To that end we consider series of fits with additional features added as constraint. These features are quantified in terms of well-known nuclear matter properties (NMP) like incompressibility K, effective mass m^*/m, symmetry energy a_{sym}, and sum-rule enhancement factor κ [4]. We study systematic variations of these NMP. Further information from giant resonances (GR) is invoked to define the optimal values for the NMP more precisely. Finally, we apply the set of SHF parametrizations thus obtained to a study of the predictive value for more detailed properties like, e.g., neutron skin, isotope shifts of charge radii, and super-heavy elements.

II. THE SKYRME ENERGY FUNCTIONAL

The goal of a nuclear mean-field theory is to describe the many-body system exclusively in terms of a set of single-particle wave functions together with the BCS occupation amplitudes $\{\varphi_\alpha, v_\alpha, \alpha = 1, \ldots, \Omega\}$. Thus the typical mean-field state is a BCS state

$$|\Phi\rangle = \prod_{\alpha>0} \left(u_\alpha + v_\alpha \hat{a}_\alpha^+ \hat{a}_{\bar{\alpha}}^+\right)|0\rangle, \tag{1}$$

where $|0\rangle$ is the vacuum state and $u_\alpha = \sqrt{1 - v_\alpha^2}$. The product runs over all pairs of time-reversed partners $(\alpha, \bar{\alpha})$ indicated by $\alpha > 0$. The mean-field equations are obtained by variation of the total energy with respect to single-particle wave functions and pairing amplitudes. The expression for the total energy is the key ingredient in the modeling. We will here employ the Skyrme energy-density functional together with a pairing functional.Both functionals are expressed in terms of a few local densities and currents: local density ρ, kinetic-energy density τ, spin-orbit density $\mathbf{J}$, current $\mathbf{j}$, spin density $\boldsymbol{\sigma}$, kinetic spin density $\boldsymbol{\tau}$, and pair current ξ. All appear twice, for protons and for neutrons, e.g., ρ_p and ρ_n. In detail they read

$$\rho_q(\mathbf{r}) = \sum_{\alpha\in q} v_\alpha^2\, |\varphi_\alpha(\mathbf{r})|^2 q \in \{\mathrm{p}, \mathrm{n}\}, \tag{2a}$$

$$\tau_q(\mathbf{r}) = \sum_{\alpha\in q} v_\alpha^2\, |\nabla\varphi_\alpha(\mathbf{r})|^2, \tag{2b}$$

$$\mathbf{J}_q(\mathbf{r}) = -\mathrm{i} \sum_{\alpha\in q} v_\alpha^2\, \varphi_\alpha^+(\mathbf{r}) \nabla \times \hat{\sigma}\, \varphi_\alpha(\mathbf{r}), \tag{2c}$$

$$\mathbf{j}_q(\mathbf{r}) = -\frac{\mathrm{i}}{2} \sum_{\alpha\in q} v_\alpha^2 \left(\varphi_\alpha^+(\mathbf{r}) \nabla \varphi_\alpha(\mathbf{r}) - \mathrm{c.c.}\right), \tag{2d}$$

$$\boldsymbol{\sigma}(\mathbf{r}) = \sum_{\alpha\in q} v_\alpha^2\, \varphi_\alpha^+(\mathbf{r}) \hat{\boldsymbol{\sigma}} \varphi_\alpha(\mathbf{r}), \tag{2e}$$

$$\boldsymbol{\tau}(\mathbf{r}) = \sum_{\alpha\in q} v_\alpha^2 \sum_{i\in\{xyz\}} \nabla_i \varphi_\alpha^+(\mathbf{r}) \hat{\boldsymbol{\sigma}} \nabla_i \varphi_\alpha(\mathbf{r}), \tag{2f}$$

$$\xi_q(\mathbf{r}) = 2 \sum_{\alpha\in q}^{\alpha>0} u_\alpha v_\alpha |\varphi_\alpha(\mathbf{r})|^2. \tag{2g}$$

It is often useful to recouple to sum and difference, e.g.,

$$\rho = \rho_{\mathrm{p}} + \rho_{\mathrm{n}}, \quad \tilde{\rho} = \rho_{\mathrm{p}} - \rho_{\mathrm{n}}, \tag{2h}$$

and similarly for all other densities and currents. The sum plays a role in the isoscalar terms of the energy functional and we will call it the isoscalar density ρ. In a similar manner, the difference plays the role of an isovector density $\tilde{\rho}$.

Our starting point is then the most general Skyrme energy functional

$$E = \int d^3r \, \{\mathcal{E}_{\mathrm{kin}} + \mathcal{E}_{\mathrm{Skyrme}}\} + E_{\mathrm{Coulomb}} + E_{\mathrm{pair}} + E_{\mathrm{cm}}, \tag{3a}$$

$$\mathcal{E}_{\mathrm{kin}} = \frac{\hbar^2}{2m_{\mathrm{p}}} \tau_{\mathrm{p}} + \frac{\hbar^2}{2m_{\mathrm{n}}} \tau_{\mathrm{n}}, \tag{3b}$$

$$\begin{aligned}
\mathcal{E}_{\mathrm{Skyrme}} = {} & \frac{B_0 + B_3\rho^\alpha}{2}\rho^2 - \frac{B_0' + B_3'\rho^\alpha}{2}\tilde{\rho}^2 + B_1(\rho\tau - \mathbf{j}^2) \\
& - B_1'(\tilde{\rho}\tilde{\tau} - \tilde{\mathbf{j}}^2) - \frac{B_2}{2}\rho\Delta\rho + \frac{B_2'}{2}\tilde{\rho}\Delta\tilde{\rho} \\
& - \frac{1}{2} B_4 \left[\rho \nabla\cdot\mathbf{J} + \boldsymbol{\sigma}\cdot(\nabla\times\mathbf{j})\right] \\
& - \frac{1}{2}(B_4 + b_4') \left[\tilde{\rho}\nabla\cdot\tilde{\mathbf{J}} + \tilde{\boldsymbol{\sigma}}\cdot(\nabla\times\tilde{\mathbf{j}})\right] \\
& + \frac{C_1}{2}(\mathbf{J}^2 - \boldsymbol{\sigma}\cdot\boldsymbol{\tau}) - \frac{C_1'}{2}(\tilde{\mathbf{J}}^2 - \tilde{\boldsymbol{\sigma}}\cdot\tilde{\boldsymbol{\tau}}),
\end{aligned} \tag{3c}$$

$$\begin{aligned}
E_{\mathrm{Coulomb}} = {} & e^2 \frac{1}{2} \int d^3r \, d^3r' \frac{\rho_{\mathrm{p}}(\mathbf{r})\rho_{\mathrm{p}}(\mathbf{r}')}{|\mathbf{r} - \mathbf{r}'|} \\
& - \frac{3}{4} e^2 \left(\frac{3}{\pi}\right)^{1/3} \int d^3r [\rho_{\mathrm{p}}]^{4/3},
\end{aligned} \tag{3d}$$

$$E_{\mathrm{pair}} = \frac{1}{4} \sum_q v_{0,q} \int d^3r \xi_q^2 \left[1 - \frac{\rho}{\rho_{\mathrm{pair}}}\right], \tag{3e}$$

$$E_{\mathrm{cm}} = -\frac{1}{2mA} \langle (\hat{P}_{\mathrm{cm}})^2 \rangle, \quad \hat{P}_{\mathrm{cm}} = \sum_i \hat{p}_i. \tag{3f}$$

Accounting for the slight difference between the proton and the neutron mass ($\hbar^2/2m_p = 20.749821, \hbar^2/2m_n = 20.721260$) becomes important for exotic and heavy nuclei. The B (B') parameters determine the strength of the isoscalar (isovector) forces. The principle Skyrme functional $\mathcal{E}_{\mathrm{Skyrme}}$ contains just the minimum of time-odd currents and densities that is required for Galilean invariance [22], namely the combinations $\rho\tau - \mathbf{j}^2$ and $\rho\nabla\cdot\mathbf{J} + \boldsymbol{\sigma}\cdot(\nabla\times\mathbf{j})$. Further conceivable time-odd couplings play a role only for odd nuclei and magnetic (unnatural parity) modes [23]. These additional time-odd terms are often derived starting with a density-dependent zero-range force. We take here the point of view of density-functional theory and start from an energy functional, choosing the minimalistic approach in the time odd channel. That modeling is similar to the strategy which is also pursued in the relativistic mean-field model [11,12,24]. The parameters B_i, B_i' are more convenient for the functional form (3). They are uniquely related to the widely used standard Skyrme parameters t_i, x_i through

$$\begin{aligned}
B_0 &= \tfrac{3}{4}t_0, \\
B_0' &= \tfrac{1}{2}t_0\left(\tfrac{1}{2} + x_0\right), \\
B_1 &= \tfrac{3}{16}t_1 + \tfrac{5}{16}t_2 + \tfrac{1}{4}t_2x_2, \\
B_1' &= \tfrac{1}{8}\left[t_1\left(\tfrac{1}{2} + x_1\right) - t_2\left(\tfrac{1}{2} + x_2\right)\right], \\
B_2 &= \tfrac{9}{32}t_1 - \tfrac{5}{32}t_2 - \tfrac{1}{8}t_2x_2,
\end{aligned}$$

$$
\begin{aligned}
B'_2 &= \tfrac{1}{16}\left[3t_1\left(\tfrac{1}{2}+x_1\right)+t_2\left(\tfrac{1}{2}+x_2\right)\right],\\
B_3 &= \tfrac{1}{8}t_3,\\
B'_3 &= \tfrac{1}{12}t_3\left(\tfrac{1}{2}+x_3\right)\\
B_4 &= \tfrac{1}{2}t_4-\tfrac{1}{2}b'_4,\\
C_1 &= \eta_{\rm tls}\tfrac{1}{8}\left[t_1\left(\tfrac{1}{2}-x_1\right)-t_2\left(\tfrac{1}{2}+x_2\right)\right],\\
C'_1 &= -\eta_{\rm tls}\tfrac{1}{16}(t_1-t_2). \qquad \text{(3g)}
\end{aligned}
$$

Note the two nonstandard entries. There is an extra parameter b'_4 for tuning the isovector dependency of the spin-orbit interaction. A zero-range two-body spin-orbit interaction leads to the fixed relation $b'_4 = t_4/2$ while a spin-orbit structure as suggested by the RMF is associated with $b'_4 = 0$ [25]. We use it here as free parameter. The tensor spin-orbit term associated with the terms $\propto C_1, C'_1$ is omitted in many parametrizations. Here we introduce a new parameter $\eta_{\rm tls}$ as a switch factor where $\eta_{\rm tls} = 1$ includes the full tensor spin-orbit and $\eta_{\rm tls} = 0$ selects the widely used option to ignore the tensor spin-orbit term. The Coulomb functional (3d) depends only on the charge density and stays outside this distinction. Its second term approximates exchange in the Slater approximation [26]. Note that we use the proton density in place of the charge density. This is a widely used, more or less standard, approximation. The center-of-mass correction (3f) is an approximation to the full center-of-mass projection [27]. It is applied *a posteriori* and its contribution to the mean-field equations is neglected. There are other recipes for the center-of-mass correction not considered here (see Refs. [4,16]). The pairing functional (3e) involves the pair current ξ and can be derived from a density-dependent zero-range force. The parameter $\rho_{\rm pair}$ determines the weight of density dependence. The limit $\rho_{\rm pair} \longrightarrow \infty$ recovers the pure δ interaction (DI) that is also called volume pairing. The general case is the density-dependent δ interaction (DDDI). A typical value near matter equilibrium density $\rho_{\rm pair} = 0.16\,{\rm fm}^{-3}$ concentrates pairing to the surface. Thus it is often denoted as surface pairing. We will consider $\rho_{\rm pair}$ as a free parameter and it will lead to an intermediate stage between volume and surface pairing.

The results of the BCS calculations depend on the space of single-nucleon states taken into account, called here pairing phase space. In fact, the cutoff is part of the pairing description. It is provided by the phase-space weights w_α in the above pairing functionals. We use here a soft cutoff profile such as, $w_\alpha = \{1+\exp[(\varepsilon_\alpha - (\epsilon_F + \epsilon_{\rm cut}))/\Delta\epsilon)\}^{-1}$, where typically $\epsilon_{\rm cut} = 5\,{\rm MeV}$ and $\Delta\epsilon = \epsilon_{\rm cut}/10$ [28,29]. This works very well for all stable and moderately exotic nuclei. For better extrapolation ability away from the valley of stability, the fixed margin $\epsilon_{\rm cut}$ may be modified to use a band of fixed particle number $\propto N^{2/3}$ instead of a fixed energy band [30]. When checking the performance of the fits for various observables (see subsection III D), we encounter also deformed configurations. These are computed with a code allowing for axially symmetric and reflection asymmetric configurations. The reflection asymmetry becomes important for fission barriers in actinides. For well-deformed nuclei, the dominant part of the correlation energy comes from angular-momentum projection. We have accounted for that at the level of the Gaussian-overlap approximation (GOA) in a form that provides correctly a smooth transition to spherical shapes where the correction vanishes [31–34]. This amounts to subtract $E_{\rm ZPE,rot} = g(\langle\hat{J}^2\rangle/4)\langle\hat{J}^2\rangle/(2\Theta_{\rm rot})$, where the interpolating function is $g(x) = x\partial_x \log\{\int_0^1 da \exp[x(a^2-1)]\}$. That correction is included in all following results dealing with deformed configurations.

III. FITTING STRATEGY

A. Global quality measure χ^2 and minimization

The free parameters of the SHF ansatz are going to be determined by a least-squares fit. To that end, we build a global quality measure by summing the squared deviations from the data as

$$\chi^2 = \sum_{\mathcal{O},{\rm nucl}} \chi^2_{\mathcal{O},{\rm nucl}}, \quad \chi_{\mathcal{O},{\rm nucl}} = \frac{\mathcal{O}^{\rm (th)}_{\rm nucl} - \mathcal{O}^{\rm (exp)}_{\rm nucl}}{\Delta\mathcal{O}_{\rm nucl}}, \tag{4}$$

where $\mathcal{O}$ stands for one of the selected observables, "nucl" for a nucleus, the upper index "th" for a calculated value, and "exp" for the experimental date. The denominator $\Delta\mathcal{O}$ stands for the *adopted* error of that observable. It renders each contribution dimensionless and regulates the relative weights of the various terms. The experimental uncertainty is of little help here because the experimental precision of these basic bulk observables is much better than what we can expect from the mean-field description, particularly for the binding energy. The limiting factor comes from theoretical uncertainties, i.e., the quality we can expect from a mean-field description. We will briefly describe the observables in subsection III B and the selection of nuclei together with the adopted errors in subsection III C.

The total quality measure is a function of all model parameters, i.e., $\chi^2 = \chi^2(p_1,\ldots,p_N)$. We search for those parameters that minimize χ^2. As standard technique we employ the χ^2 minimization technique from Bevington [35,36], complemented occasionally by Monte Carlo sampling to enhance the chances for ending up in the global minimum.

The aim of this publication is to explore systematically the various influences from key features as, e.g., incompressibility or symmetry energy. We thus add constraints on such key features. That is done most simply by adding the wanted features as additional observables with very small adopted errors $\Delta\mathcal{O}$ to the χ^2.

The rules of χ^2 fitting also provide information to estimate the statistical errors for extrapolations to other observables. Let us consider some observable A. Its expectation value is a function of the model parameters, i.e., $A = A(p_1,\ldots,p_N)$. The extrapolation error then becomes

$$\Delta A = \sqrt{\sum_{i,j}\frac{\partial A}{\partial p_i}(\mathcal{C}^{-1})_{ij}\frac{\partial A}{\partial p_j}}, \quad \mathcal{C}_{kl} = \frac{\partial^2\chi}{\partial p_k \partial p_l}. \tag{5}$$

That is the allowed variation of the observable A within the ellipsoid of $\chi^2 - \chi^2_{\rm min} \leqslant 1$, i.e., for all χ^2 that stay at most one unit above the minimum. We will exploit that feature to compute extrapolation errors for all observables not included in the fit data.

B. Selection of fit observables

The total binding energy E_B of a nucleus is the most immediate observable in self-consistent mean-field models. It is naturally provided by the numerical solution of the mean-field equations. The next important observables are related to the spatial extension of the nucleus. It can be accessed experimentally through elastic electron scattering that yields the nuclear charge form factor $F_{\mathrm{ch}}(q)$ and by Fourier transformation the nuclear charge density $\rho_{\mathrm{ch}}(r)$ [37]. SHF calculations yield first the proton and neutron densities that need to be folded with the intrinsic electromagnetic structure of the nucleons to obtain the charge density and charge form factor [38]. Mean-field models provide reliable information about the form factor at low momentum q [39,40]. This region of the form factor at low momentum can be described by three parameters [37], the r.m.s. radius

$$r_{\mathrm{rms}}^2 = -\frac{3}{F_{\mathrm{ch}}(0)}\frac{d^2}{dq^2}F_{\mathrm{ch}}(q)\bigg|_{q=0}, \tag{6}$$

the (first) diffraction radius

$$R = \frac{4.493}{q_0^{(1)}}, \tag{7}$$

which is determined from the first zero of the form factor $F_{\mathrm{ch}}[q_0^{(1)}] = 0$, and the surface thickness

$$\sigma^2 = \frac{2}{q_m}\log\left[\frac{F_{\mathrm{box}}(q_m)}{F_{\mathrm{ch}}(q_m)}\right], \quad q_m = 5.6/R. \tag{8}$$

Therein $F_{\mathrm{box}}(q)$ corresponds to the form factor of a homogeneous box of radius R, i.e., $F_{\mathrm{box}}(q) = 3j_1(qR)/(qR)$. The diffraction radius parameterizes the overall diffraction pattern that resembles that of a box of radius R. It is the box-equivalent radius. For more details find a recent summary in Ref. [4].

The most prominent observable for $T = 1$ pairing correlations on the mean-field level is the odd-even staggering of nuclear masses from which an approximation to the pairing gap can be extracted, e.g., using a five-point formula yields for the neutron gap

$$\begin{aligned}\Delta_n^{(5)} = &-\tfrac{1}{8}E(Z,N+2) + \tfrac{1}{2}E(Z,N+1) - \tfrac{3}{4}E(Z,N)\\ &+\tfrac{1}{2}E(Z,N-1) - \tfrac{1}{8}E(Z,N-2)\end{aligned} \tag{9a}$$

and similarly for the proton gap $\Delta_p^{(5)}$. The computation of odd nuclei using mean-field models, however, is very involved. It requires deformation and a long search for the optimum blocked configuration that increases numerical expense by two orders of magnitude. Thus it is not well suited for systematic surveys. One can compute an average pairing gap from the state-dependent gap Δ_α using a weight that is sensitive to the region about the Fermi surface [30,41,42]

$$\bar{\Delta}_q = \frac{\sum_{\alpha\in q} u_\alpha v_\alpha \Delta_\alpha}{\sum_{\alpha\in q} u_\alpha v_\alpha} \qquad (\alpha > 0). \tag{9b}$$

These spectral gaps $\bar{\Delta}_q$ are found to be fairly well related to the five-point gaps $\Delta_q^{(5)}$ in midshell regions [30,42]. For magic nuclei and next to them, these two quantities develop very differently [43]. There remains some influence from nuclear shape fluctuations on $\Delta_q^{(5)}$ [44] that gives an uncertainty of about 10–20% for the comparison of the two different definitions (10) for a gap.

We also need some information that is specific to the spin-orbit terms in SHF. The obvious quantity for the purpose are the l*s splittings of single-particle energies. Experimental information on single-particle energies of even-even nuclei is drawn from the single-nucleon removal energies or from the low-lying excited states of the adjacent odd-A nuclei. That identification requires that the polarization effects induced by the extra nucleon (or hole) are small. The magnitude of these effects have been investigated for doubly magic nuclei by Ref. [45] within the RMF and Ref. [46] with SHF using the linear response theory. It is found that energy differences among particle states and hole states separately are robust. Thus spin-orbit splittings are a robust signal as long as they do not cross the shell gap. Furthermore, the involved single-particle energies should not be too far away from the Fermi energy to keep perturbation from higher configurations (additional 1ph couplings) low. Another limitation has to be considered for states in the particle spectrum because the state should stay safely off the particle continuum. Thus we decide to include only spin-orbit splittings of hole states close to the Fermi energy in doubly magic nuclei. The chosen data are listed in Tables III and IV.

C. Correlation effects and adopted errors

The goal is to adjust an effective nuclear energy-density functional. The observables and nuclei included in the adjustment should be well adapted for a pure mean-field description. Thus we have to scrutinize the most dominant effects going beyond mean field. As pointed out in the Introduction, the strong short-range correlations as well as correlations from resonances and high modes follow a trend smooth in nucleon numbers Z and N and can be assumed to be effectively incorporated into the energy-density functional [40]. We have to care, however, about correlation effects that vary strongly within the chart of isotopes. These stem predominantly from the low-lying quadrupole excitations, associated with large-amplitude collective motion like soft vibrations and rotations; for extensive recent analysis see Refs. [19–21]. We are concerned here with the influence of correlations on bulk observables, the change in energy $\delta E_{\mathrm{corr}} = E_{\mathrm{corr}} - E_{\mathrm{mf}}$ (where E_{corr} is the energy from the correlated calculation and E_{mf} the mean-field result), and similarly the changes δr in charge r.m.s. radii, δR in diffraction radii, and $\delta\sigma$ in surface thickness.

A good chance for small correlation effects exists for semimagic nuclei where either the proton or the neutron number corresponds to a shell closure. These nuclei are generally spherical. Figure 1 summarizes the correlation effects on binding energies (lower panels) and radii as well as surface thicknesses (upper panels). The results were obtained with the parametrization SkI3 [25]. Other parametrizations yield very similar results [21] such that Fig. 1 is a typical result for the error distribution for any reasonable Skyrme force. The correlation effects generally shrink with increasing system size, which is expected because low-lying excitation energies generally decrease. It is a bit surprising, however, that

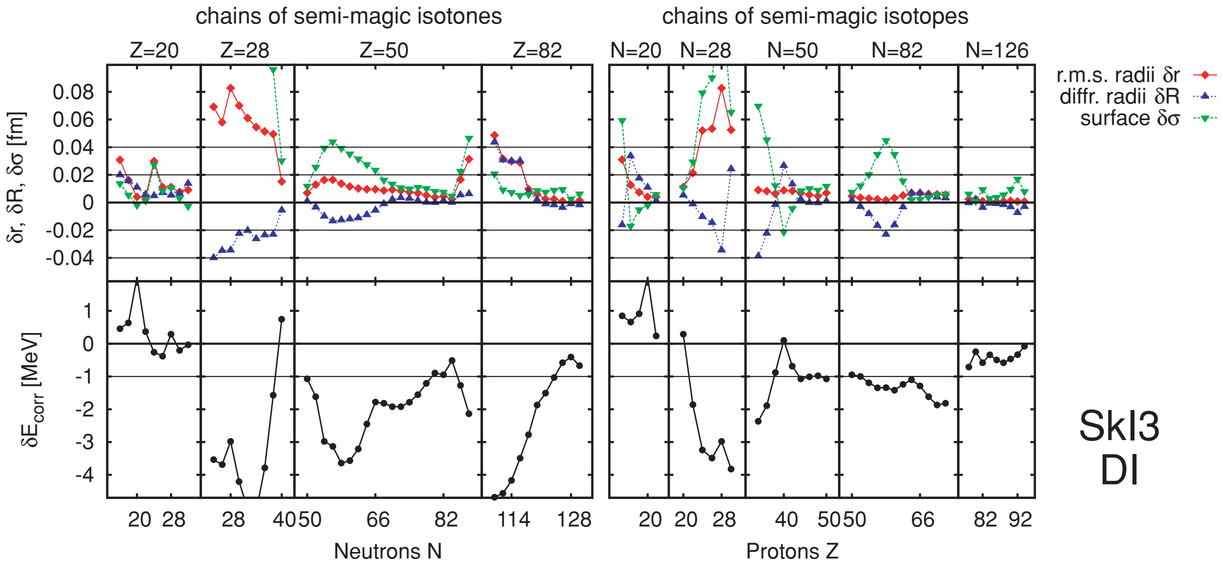

FIG. 1. (Color online) Correlation effects on semimagic isotopic (left) and isotonic (right) chains computed with SkI3 and DI pairing. The isotopic chains are $Z = 20$, $Z = 28$, $Z = 50$, and $Z = 82$, and the isotonic chains $N = 20$, $N = 28$, $N = 50$, $N = 82$, and $N = 126$. (Upper panels) Correlation shifts of charge r.m.s. radii (δr), diffraction radii, (δR), and surface thicknesses ($\delta\sigma$). (Lower panels) Correlation energies (δE_{corr}). Horizontal dotted lines indicate intended error limits.

the correlation energies in isotopic chains can grow so large in the midshell region. The hitherto often underestimated isotonic chains are visibly less perturbed. Light nuclei generally show larger fluctuations, sometimes even acquiring unphysically positive correlation energies. The small positive values about 0.2–0.5 MeV are still within the precision of our method and imply practically negligible correlation energies. The only exception is ^{40}Ca at ($Z = N = 20$). The unreasonably large value is due to the fact that the 2^+ mode is not really collective in that nucleus [21] but that we compute correlations using the GOA that is not necessarily valid for noncollective modes. This unphysical case, however, is in any case excluded from the fit data set due to the Wigner effect (for $N = Z$) [47].

The faint horizontal lines in Fig. 1 indicate the error bands associated with the adopted errors, 1 MeV for E_B, 0.04 fm for R_{diff} and σ, and 0.02 fm for r_{rms}. Observables that stay below these limits are included in the fit data. Points that are outside the desired error bands, but not too far away, are included with degraded error weight that is done by multiplying the general adopted error $\Delta\mathcal{O}$ for that nucleus with a certain factor depending on how large the expected correlation could be. Moreover, all nuclei with $N = Z$ are excluded already because they carry a correlation contribution from the Wigner energy [47] and we do not yet have reliable means to compute that correction. The choice of fit data thus deduced is listed in Tables III and IV. One finds therein also the values for pairing gaps and spin-orbit splittings. We have no reliable estimate for the errors in these observables. The pairing gap is deduced from the five-point difference of binding energies [30]. The pairing gaps for nuclei whose energy has degraded error weight are modified by the same degradation factor for reasons of consistency. The overall error is tuned such that the r.m.s. average χ from all pairing gaps is of the same order as for the other observables. A similar strategy taking over weight factors from binding energies is applied for the spin-orbit splittings. Altogether this amounts to an adopted error of 0.12 MeV for the gaps and 10% for the spin-orbit splittings; for details see again Tables I and II. Correlation energies are always negative (the few exceptions at low A are defects) and r.m.s. radii always grow, but the fits produce an average with deviations lying on both sides. One would very much like to leave a margin for correlations. A safe construction would require a deeper knowledge of the systematics of correlation effects and development of simple estimates of them. At the present stage, we to fit to straightforward mean-field results and refrain from adding empirical corrections.

TABLE I. Global quality measures for various classes of observables as achieved with the parameterization SV-min. The second column shows the contribution from an observable to χ^2 while the third column expresses this as χ^2 per data point. The last column produces the r.m.s. errors as such and the numbers in brackets indicate the adopted error taken as weights for the fit; see Eq. (5).

	χ^2	χ^2/point	r.m.s. error	
Binding energy E_B	12.07	0.17	0.62 MeV	(1.0)
Diffr., radius R	11.18	0.40	0.029 fm	(0.04)
Surface thick. σ	4.22	0.26	0.022 fm	(0.04)
r.m.s. radius r	15.86	0.32	0.014 fm	(0.02)
Pairing gap Δ_p	4.27	0.25	0.11 MeV	(0.12)
Pairing gap Δ_n	2.43	0.15	0.14 MeV	(0.12)
l·s splitting	3.18	0.45	0.25%	(20)
Total	53.22	0.26		

TABLE II. NMP as defined in subsection III E for the for the various SHF parameterizations used in this article (K in MeV, a_{sym} in MeV, E/A in MeV, ρ_{eq} in fm^{-3}, a'_{sym} in MeV fm^3, m^*/m dimensionless, and κ dimensionless). The rightmost column lists the global quality measure χ^2. The parameterization SV-min results from an unconstrained minimization of the total quality measure χ^2 according to Eq. (5) with the data and adopted errors from Tables I and II. The other parameterizations were obtained by a fit constrained on four NMP. SV-bas is the base point of the systematic variation with the constraints: $K = 234$ MeV, $m^*/m = 0.9$, $a_{\mathrm{sym}} = 30$ MeV, and $\kappa = 0.4$. From that point, one property is varied, the incompressibility K (via power of density dependence α) in SV-K, the effective mass in SV-mas, the symmetry energy in SV-sym, and the sum-rule enhancement in SV-kap. Finally, SV-tls is constrained like SV-bas but employs the full tensor spin-orbit terms. Moreover, we append to the list the NMP for the four conventional Skyrme forces used in several comparisons.

Force	K	m^*/m	a_{sym}	κ	ρ_{eq}	E/A	a'_{sym}	χ^2
SV-min	222	0.95	30.7	0.08	0.1610	−15.91	93	53.2
	±8	0.15	1.4	0.40	0.0013	0.06	89	
SV-bas	234	0.9	30	0.4	0.1596	−15.90	68	57.9
SV-K218	218	0.9	30	0.4	0.1615	−15.90	72	57.0
SV-K226	226	0.9	30	0.4	0.1605	−15.90	71	56.3
SV-K241	241	0.9	30	0.4	0.1588	−15.91	65	61.3
SV-mas10	234	1.0	30	0.4	0.1594	−15.91	59	60.8
SV-mas08	234	0.8	30	0.4	0.1597	−15.90	84	59.5
SV-mas07	234	0.7	30	0.4	0.1500	−15.89	109	68.0
SV-sym28	234	0.9	28	0.4	0.1595	−15.86	15	63.4
SV-sym32	234	0.9	32	0.4	0.1595	−15.94	119	58.0
SV-sym34	234	0.9	34	0.4	0.1592	−15.97	169	61.6
SV-kap00	234	0.9	30	0.0	0.1598	−15.90	82	52.6
SV-kap20	234	0.9	30	0.2	0.1597	−15.90	74	56.5
SV-kap60	234	0.9	30	0.6	0.1595	−15.91	61	60.5
SV-tls	234	0.9	30	0.4	0.1595	−15.89	69	61.2
SkM*	217	0.79	30	0.53	0.1602	−15.75	95	
SLy6	230	0.69	32	0.25	0.1590	−15.92	100	
SkI3	258	0.58	35	0.25	0.1577	−15.96	212	
BSk4	237	0.92	28	0.18	0.1575	−15.77	27	

D. More detailed observables

There are many more nuclear properties that are interesting to look at but that are not yet suited for inclusion in a systematic fit, because the relation to experimental data is somewhat uncertain (neutron radii, giant resonance frequencies, fission barriers) or too cumbersome to compute (low-lying collective states). We will look at several such observables *a posteriori*: the neutron skin in ^{208}Pb, the isotope shift of charge radii between ^{214}Pb and ^{208}Pb, the neutron level sequence near the Fermi surface in ^{132}Sn, extrapolation to super-heavy elements (SHE), and GR. Some of these observables, namely the GR resonance peak frequencies, are even used as additional selection criteria. We will now explain their computation, whereas the other observables are introduced in later sections.

The dominant excitation modes of the nucleus are the GRs. Their average peak position can be related to basic features. Heavy nuclei show least spectral fragmentation and are best suited for evaluating these averages. We will consider GR in ^{208}Pb, in particular the isoscalar giant monopole resonance (GMR), the isovector giant dipole resonance (GDR), and the isoscalar giant quadrupole resonance (GQR). The spectral strength distribution is computed by the random-phase approximation (RPA) done self-consistently with the same Skyrme interaction as was used for the ground state, for technical details see Refs. [39,48]. We use a large phase space on a large spherical grid of 30 fm radius to achieve a sufficiently fine discretization of the continuum [49] for subsequent folding with a Lorentzian of frequency dependent width $\Gamma = \max[(\hbar\omega - 8\,\mathrm{MeV})/3.5\,\mathrm{MeV}, 0.1\,\mathrm{MeV}]$. The linear ω dependence starts at neutron emission threshold with an empirically adjusted slope. It simulates the escape width and to some extent the collisional width. The strengths in ^{208}Pb all have one unique peak in the GR region frequency that can easily be read off. Comparison with the experimental data will be done with respect to that GR peak frequency. The experimental values are $\hbar\omega_{\mathrm{GMR}} = 13.7\,\mathrm{MeV}$, $\hbar\omega_{\mathrm{GDR}} = 13.6\,\mathrm{MeV}$, and $\hbar\omega_{\mathrm{GQR}} = 10.9\,\mathrm{MeV}$ [50–52].

E. Nuclear matter properties

Homogeneous nuclear matter describes the leading contributions (volume terms) to nuclear properties. They are considered as useful pseudo-observables characterizing the bulk properties of effective interactions. There exist close relations between such bulk properties and certain combinations of Skyrme parameters, but it is often more instructive to discuss a parametrization in terms of these NMP. When performing systematic variations of forces, we will consider a scan of dedicated values for selected NMP rather than simple Skyrme parameters.

The leading quantity is the energy per particle $(E/A)(\rho)$, often called equation of state. Its minimum $(E/A)_{\rm eq}$ at saturation density $\rho_{\rm eq}$ defines the volume energy, related to the equilibrium state of nuclear matter. Energy and density in finite nuclei are modified by surface and shell effects but always stay close to these guiding values. Furthermore, we discuss NMP related to excitations (zero sound). The incompressibility at the saturation point is given by

$$K_\infty = 9\,\rho^2 \,\frac{d^2}{d\rho^2}\,\frac{E}{A}\bigg|_{\rm eq}\,, \tag{10}$$

where $\rho = \rho_n + \rho_p$ is the total density. It corresponds to the curvature at the minimum and is related to breathing modes like the giant monopole resonance [53]. The symmetry energy coefficient is related to the isovector curvature at the saturation point

$$a_{\rm sym} = \frac{\rho^2}{2}\,\frac{d^2}{d(\rho_n-\rho_p)^2}\,\frac{E}{A}\bigg|_{\rm eq}\,. \tag{11}$$

Finite nuclei are also sensitive to smaller densities whose symmetry energy is characterized additionally by the slope

$$a'_{\rm sym} = \frac{d}{d(\rho_n-\rho_p)}a_{\rm sym}. \tag{12}$$

The isoscalar effective mass m^* is calculated as

$$\frac{\hbar^2}{2m*} = \frac{\hbar^2}{2m} + \frac{\partial}{\partial\tau}\,\frac{E}{A}\bigg|_{\rm eq}\,. \tag{13}$$

The isovector effective mass is usually expressed as the enhancement factor of the Thomas-Reiche-Kuhn sum rule [54], which reads

$$\kappa_{\rm TRK} = \frac{2m}{\hbar^2}\,\frac{\partial}{\partial(\tau_n-\tau_p)}\,\frac{E}{A}\bigg|_{\rm eq}\,. \tag{14}$$

Note the subtle difference between total derivatives in Eqs. (10) and (11) and partial derivatives in Eqs. (13) and (14). The latter take E as written in the Skyrme functional (3a) considering all densities and currents $(\rho, \tau, \ldots)$ as independent variables while the total derivative first expresses all quantities in terms of the actual Fermi momentum $k_F = k_F(\rho)$, and thus the density, before performing the derivative, e.g., considering $\tau \longrightarrow \tau(\rho)$.

IV. RESULTS AND DISCUSSION

In this section, we will present the parametrizations obtained by adjustment to the above selected set of data, optionally with an additional constraining condition. The aim of the survey is to explore the influence of varying conditions in a systematic manner. We thus name the forces with the header "SV" and add different three digits qualifiers to indicate the constraint for which a force was adjusted. As outlined in Sec. II, the Skyrme energy functional leaves some options to choose. The practical consequences thereof will be discussed in subsection IV D. As a result, we will employ the following standard choices: The tensor spin-orbit is omitted, i.e., $\eta_{\rm ls} = 0$, whereas isovector spin-orbit coupling b'_4 and the cutoff density in the DDDI recipe $\rho_{\rm pair}$ are allowed as free parameters in the fits.

Furthermore, we will often compare with a few typical parametrizations from the existing literature: SkM* as a widely used, meanwhile somewhat obsolete, old standard [55]. It belongs to the second generation of Skyrme forces that for the first time delivered a high-precision description of nuclear ground states (as compared to the first generation forces). It was developed with an explicit study of surface energy and fission barriers in semiclassical approximation. The set SLy6 and its cousins have been developed with a bias to neutron-rich nuclei and neutron matter aiming at astrophysical applications [56]. SkI3 (and SkI4) exploit the freedom of an isovector spin-orbit force to obtain an improved description of isotopic shifts of r.m.s. radii in neutron-rich Pb isotopes that posed a severe problem to all conventional Skyrme forces [25]. Finally, we consider one representative of the series of forces started in Ref. [17]. These forces are fitted predominantly to binding energies but employ an huge pool of nuclei including odd and deformed ones. For deformed nuclei a simple correction for the angular-momentum projection was added, and an *ad hoc* correction for the Wigner energy in $N = Z$ nuclei [47] was applied. All these forces are are of comparable quality with respect to the reproduction of the binding energies of finite nuclei. They differ in details of treatment or boundary conditions. We choose here the force BSk4 from Ref. [57] because it has an effective mass of $m^*/m = 0.92$ that comes close to the typical values of our fits.

A. Unconstrained fits

1. The fit to standard data: SV-min

In a first round, we follow the most straightforward strategy and adjust the model parameters to the data as selected in the previous section and detailed in Tables I and II, without any additional constraint. The result is called the parametrization "SV-min"; for its detailed model parameters see Table V. Figure 2 shows the deviation from the given data for each observable and nucleus. All results stay fairly well within the chosen error bands. That holds even for the points fitted with lower weight (open circles). In fact, the error bands are not fully exhausted and the r.m.s. errors stay safely below the adopted errors. The bands are generally filled on both sides of the zero line, which means that the fit averages nicely through the deviations. An exception is here the diffraction radius (second panels from below), where the deviation is always positive which indicates that this observable is not easy to adjust within the given model. The theoretical results are (within the allowed errors) systematically larger than the experimental data. Only a few points exist for the spin-orbit splitting (uppermost panel) and these do not fit as nicely as the other observables, even with a low demand such as a 20% r.m.s. error. This indicates that the single-particle structure is a very demanding observable. We will see that again for other level sequences later.

The global quality measures for the fit SV-min are shown in Table I. The r.m.s. errors (last column) show again what we have seen in Fig. 2, namely that energies and form parameters (radii, surface thickness) perform very well, better than the adopted errors as estimated from expected correlation effects.

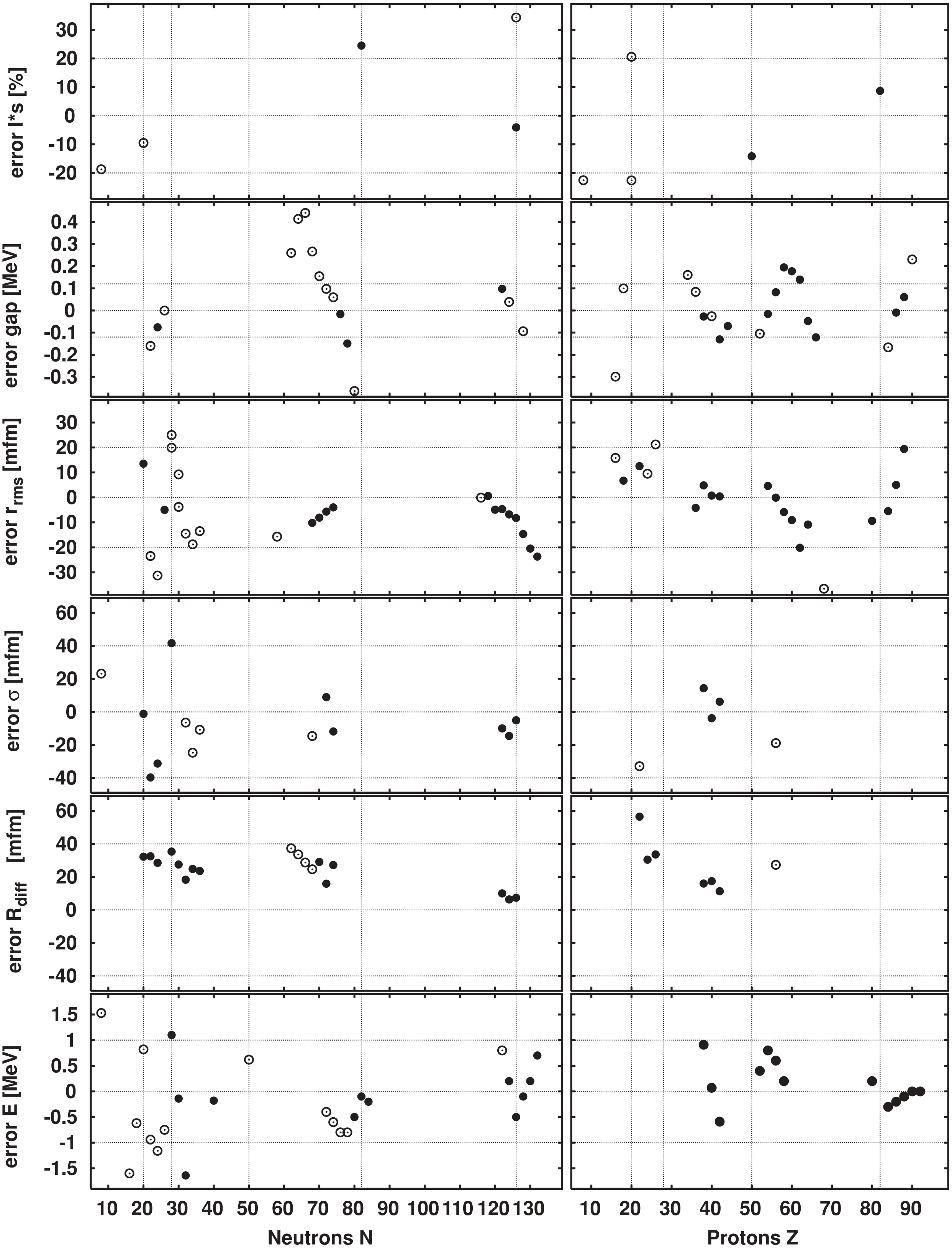

FIG. 2. Deviation from experimental data for the nuclei and observables in the fit sample as listed in Tables III and IV. The results are drawn versus N for the isotopic chains (left) and versus Z for the isotonic chains (middle). The values 0 (perfect matching) and the adopted error bands are indicated by dotted horizontal lines. Filled circles indicate data points fitted with full weight while open circles stand for data points with reduced weight (weight factor >1 in Tables III and IV). Results are shown for the parametrization SV-min resulting from a straightforward, unconstrained fit to the data.

It seems that a part of the correlations can be accounted for by the model parameters. Pairing gaps are just at the wanted limits and the l·s splittings are somewhat at the edge. The good overall performance yields a very low total χ^2 as can be seen from the very small χ^2 per data point of about 1/4. Typical fits aim at a value of 1. The strict rules of χ^2-fitting would allow reduction of the adopted errors until a χ^2 per data point of one is reached. We do not pursue that strategy here because our adopted errors are determined by the expected reliability of mean-field models from estimating correlation effects. The fact that χ^2 per data point comes out much lower than one indicates the enormous versatility of the Skyrme energy functional to describe global ground-state properties.

To check the interpolation and extrapolation properties, we show in Fig. 3 the errors in binding energies and r.m.s. radii throughout all known nuclei, including deformation. The energies are displayed in two ways. The lowest panel shows the energies as they result straightforwardly from the mean-field calculations (including center-of-mass correction). The fit nuclei (filled squares) perform very well while large deviations can develop for other nuclei. Note that the majority of deviations is positive, which indicates that additional binding through correlation energies would correct in the desired direction. For well-deformed nuclei, the dominant part of the correlation energy comes from angular-momentum projection. We have accounted for that at the level of the GOA [21,31,32]. The results with angular-momentum projection are shown in the middle panel of Fig. 3. The deformed nuclei up to Pb now perform very well. The remaining discrepancies in the region $A < 210$ are very likely missing correlations. This means that the fit interpolates nicely for all these nuclei provided soft nuclei are computed with quadrupole ground-state correlations. However, for actinides and SHE, the trend of the deviations is too strong to be cured by remaining vibrational correlations. The extrapolation to deformed super-heavy elements is plagued by a growing trend to underbinding. We will take up that question later on. The results for the r.m.s. radii look pleasant. The larger deviations for some soft nuclei may still be cured by correlations. There are not yet enough data to read off a trend for super-heavy elements. The uppermost panel shows the difference between theoretical and experimental proton deformations as derived from the $B(E2)$ values. They are given as dimensionless quadrupole moments associated with the operator $\hat{\beta} = \hat{Q}_{20}\sqrt{\pi}/(\sqrt{5}Ar^2)$, where r is the r.m.s. radius and $\hat{Q}_{20} = r^2 Y_{20}$ the spherical quadrupole operator. The theoretical values include the quadrupole variance, i.e., $\beta^{\mathrm{B(E2)}}_{\mathrm{theo}} = \sqrt{\langle\hat{\beta}^2\rangle} = \sqrt{\langle\hat{\beta}\rangle^2 + \langle\Delta^2\hat{\beta}\rangle}$. It is to be remarked that this variance from the mean-field ground state underestimates the true variance for soft vibrators and transitional nuclei. This lets us expect huge deviations for the majority of nuclei and this is indeed seen in the results. However, the picture looks better for rather rigid spherical nuclei with small correlations (our fit nuclei) and well-deformed nuclei. It is a surprisingly nice agreement in view of the fact that sizable contributions to the variance from the true collective ground state are still missing.

Further properties of SV-min will be discussed later in connection and comparison with other parametrizations.

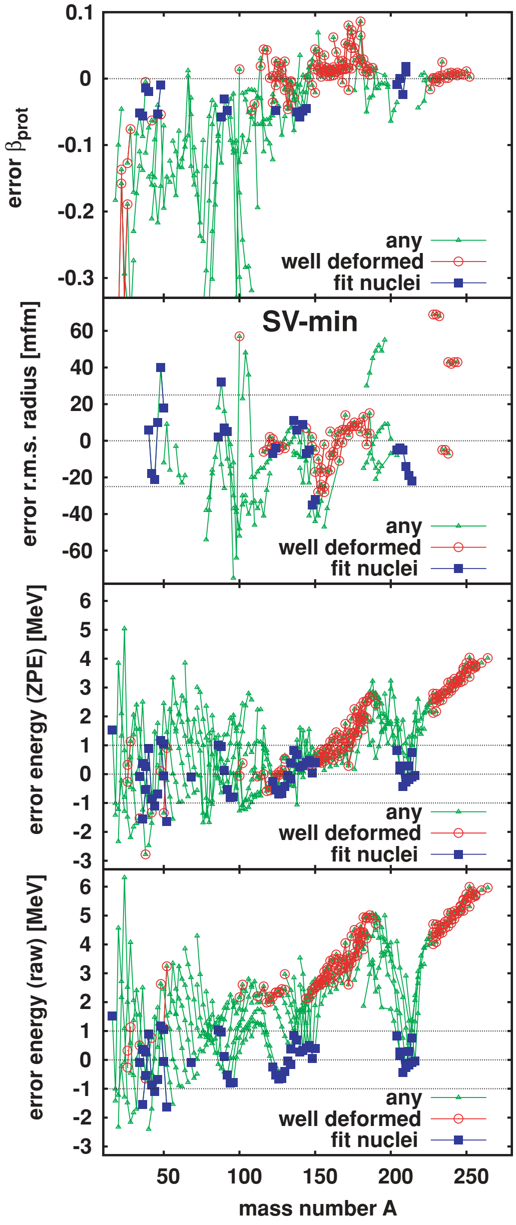

FIG. 3. (Color online) Errors in binding energies (lower two panels), r.m.s. radii (second from above), and proton deformation throughout all nuclei for which experimental data were available. The lowest panel uses the pure (deformed) mean-field value for the binding energies while angular-momentum projection is accounted for in the middle panel. The experimental deformations are deduced from electromagnetic $B(E2)$ values [58] and are compared with the quadrupole variances (see Sec. III D). For energies and radii, the nuclei that were included in the fit are marked by filled squares, well-deformed nuclei by open circles, and all others by triangles.

2. A fit including a super-heavy nucleus

We have seen above that the fitted force performs satisfying for interpolations but not so well for extrapolations. This suggests to extend the range of interpolation by adding super-heavy nuclei to the pool of data. Thus we have performed

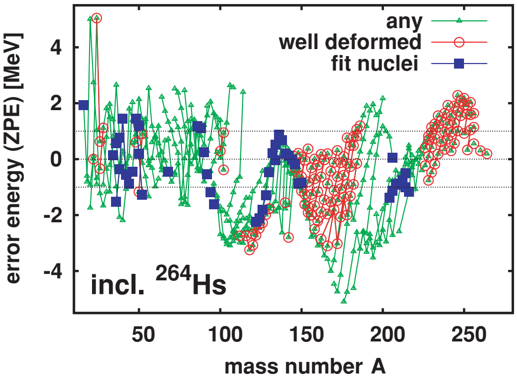

FIG. 4. (Color online) Errors in binding energies (including center-of-mass correction and angular-momentum projection in GOA) throughout all nuclei for a parametrization where the binding energy of ^{264}Hs was additionally included in the χ^2.

a fit where the binding energy of ^{264}Hs was added with high weight to the standard set of data. That nucleus is well deformed. The angular-momentum projected energy has been taken as reference value for the fit. The results for the performance on energies are shown in Fig. 4. The error for ^{264}Hs has successfully been curbed down to almost zero. But that is achieved at the price of lowering all energies for medium-heavy and heavy nuclei. The performance for the fit nuclei is visibly degraded and other nuclei are turned to overbinding, leaving no space for possible correlation energies. We obviously encounter a deep-rooted problem with the given Skyrme energy functional when considering the overall binding energy of SHE. The discussion of SHE will be continued in subsections IV E6 and IV E7.

B. Fits with constraints on NMP

1. *Variation of NMP*

The uppermost entry of Table II shows the NMP and the final χ^2 for SV-min together together with its extrapolation uncertainties computed according to Eq. (6). The χ^2 is very small in view of about 200 given data points. The NMP are more or less in commonly accepted ranges as used, e.g., in the liquid-drop model [59]. The "ground-state" properties, equilibrium density $\rho_{\rm eq}$, and binding energy E/A are well fixed while all the other NMP related to excitations show sizable uncertainties. The fit leaves some freedom in these respects. Moreover, we will see that the most prevailing nuclear excitations, the GRs, are not all so well tuned in SV-min. This suggests to exploit the freedom left by the χ^2 fits for a fine tuning of GR. Moreover, it is interesting as such to explore the large space of still allowed variations. To that end, we perform fits to the given set of data where additionally four NMP are kept fixed: incompressibility K, effective mass m^*/m, symmetry energy $a_{\rm sym}$, and sum-rule enhancement factor κ (see subsection III E for its definition). The first two are isoscalar properties and the last two isovector. One may wonder why the slope of the symmetry energy, $a'_{\rm sym}$, is not included in the variation. The reason is that $a'_{\rm sym}$ is tied up very closely to $a_{\rm sym}$ by the fits such that only one of both shows that freedom of choice.

A four-dimensional landscape of variations of NMP is too bulky to handle. We prefer to define one "base point" about which we perform variation of one NMP at a time thus dealing with four sets of variations. For the choice of the base point, we exploit the full space of variations in the four NMP and use the freedom to accommodate the GR properties as well as possible (see subsection IV C). Including additional information from GR (see subsection IV C), we find the following choice a good compromise: $K = 234$ MeV, $m^*/m = 0.9$, $a_{\rm sym} = 30$ MeV, and $\kappa = 0.4$. The corresponding parametrization is called "SV-bas." We then vary each one of the four NMP while keeping the other three at the base value. This yields four sets of variations with prefix SV-K for varied K, SV-mas for varied m^*/m, SV-sym for varied $a_{\rm sym}$, and SV-kap for varied κ. Table II shows the NMP for these parametrizations and the detailed parameters for the functional (3a) are provided in Table V in Appendix. There is also one parametrization SV-tls with the base values for NMP but now including tensor spin orbit, i.e., $\eta_{\rm tls} = 1$. This serves to explore the effect of the tensor spin-orbit term by comparison with SV-bas.

The overall quality measure χ^2 is shown in the rightmost column of Table II. The constraints, of course, degrade the quality a bit. But we see that the variations yield χ^2 that stay within an acceptable range of about 10% increase in χ^2. As we will see in subsection IV C, SV-bas performs much better than SV-min for GR in ^{208}Pb. That counterweights the small losses on the side of ground-state properties.

The NMP as given in Table II characterize ground states and excitation properties for modes with natural parity. As typical representatives for excitations with unnatural parity, we have also checked spin modes in nuclear matter. These can be characterized by the Landau parameters g_0 for pure spin excitations and g'_0 for a spin-isospin mode [60]. Taking up the formula as given in Ref. [23], we have computed these Landau parameters for the energy functional (3a). The only contribution comes from the tensor spin-orbit term. Thus we have $g_0 = 0 = g'_0$ for all forces with $\eta_{\rm tls} = 0$. Only SV-tls has a nonvanishing tensor spin-orbit term. For that force we find $g_0 = -0.73$ and $g'_0 = 0.191$. These numbers stay safely above the critical value for spin(-isospin) instability. Thus all forces introduced here are stable in the spin channels. Note that we are here using the energy functional with minimal time-odd terms, namely just those that are required to achieve Galilean invariance. That leaves the effective interaction in all channels much more robust. Thus one should not be puzzled by the rather large negative values for the spin-exchange parameters x_1 and x_2 in Table V. These come from expressing the functional in terms of the conventional Skyrme parameters, mediated through Eq. (4). Spin stability is guaranteed in connection with the functional (3a). A different picture would evolve when taking the Skyrme force literally as a zero-range force. This yields additional terms in the spin channel that can easily render a parametrization unstable in the spin channel. However, from an energy-density functional viewpoint, we see no compelling reason to include those terms.

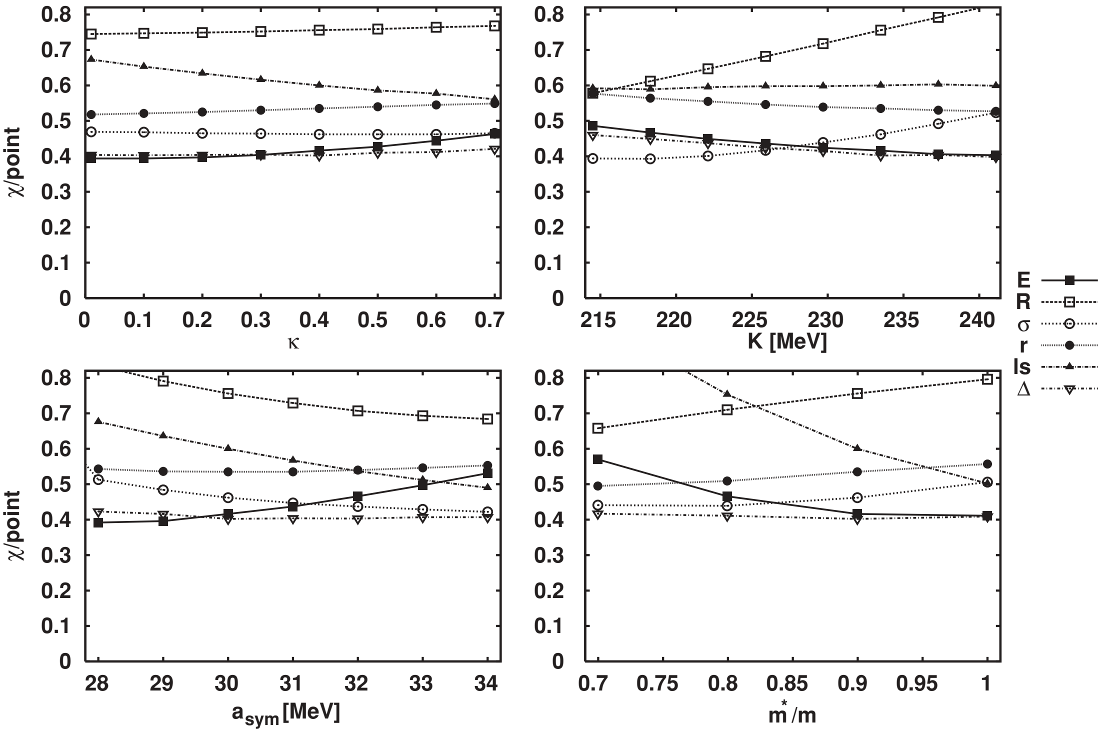

FIG. 5. The distributions χ_{obs} for each observable as indicated for four cases of systematically varied bulk parameters. (Lower left) Variation of symmetry energy a_{sym}; (upper left) variation of sum-rule enhancement κ; (lower right) variation of effective mass m^*/m; (upper right) variation of incompressibility.

2. *Trends of the errors*

The quality measure χ^2 is composed of different observables whose relative weight is determined by the given adopted errors. It is known from earlier studies that the choice of observables has an influence on extrapolated NMP (see, e.g., Ref. [36]). The sets with systematically varied NMP now allow to visualize these trends. Figure 5 shows the r.m.s. averaged χ_{obs} per data point for each observable separately. The figure has four panels to show the trends with respect to the four NMP variations considered: incompressibility K, effective mass m^*/m, symmetry energy a_{sym}, and sum-rule enhancement κ. Variation of sum-rule enhancement κ changes very little in all observables. That feature is only loosely determined by the data set, as already seen in Table II from the rather large uncertainty for SV-min. We will need further conditions to make a more definite choice. The other three features lead all to sizable trends but often lead in different directions. For example, the lower right panel shows that the r.m.s. radii would prefer low values of m^*/m while the energy prefers $m^*/m \approx 0.9$ and other observables even higher values of m^*/m. The final "optimum" for m^*/m depends very much on the choice of the relative weight of the different observables. Even within the energy as observable, we could revert the trend when giving light nuclei more weight by using relative errors [36] rather than absolute errors as done here. Significantly different trends are seen also for variation of a_{sym} and K. It is thus obvious that the relative weights in the composition of the χ^2 determine the final extrapolated NMP. Note that the actual changes in the contributions to χ^2 are small such that the total χ^2 varies only very little when scrolling through the different NMP. There is a broad choice of well performing parametrizations. This explains why there are so many different SHF paetrizations around which all provide a good description of nuclear ground-state properties but vary in several of the key features. In other words, the strategy of χ^2 fitting leaves several vaguely determined aspects. One needs to include further observables that are more specific to the open features.

C. Information from giant resonances

1. *GR in* ^{208}Pb *and its relation to NMP*

Figure 6 collects results for the peak frequencies of the GR in ^{208}Pb and of the GDR in ^{16}O. We concentrate first on discussing the GR in ^{208}Pb. The results for the straightforward fit SV-min are mixed. The GQR fits nicely, the GMR lies slightly to low, and the GDR is far off the goal. The uncertainties (see error bars for SV-min) are sufficiently large such that a good reproduction of GR in ^{208}Pb seems within the reach of allowed variations.

The relation between NMP and GR properties becomes apparent from the various chains of the systematically varied forces. The situation is particularly simple for the isoscalar excitations. There is a unique relation between an isoscalar GR and isoscalar NMP: the GMR is sensitive exclusively to K and the GQR to m^*/m. Both these GR show a clean excitation spectrum with one peak. Thus we use these two data points to fix the otherwise weakly determined isoscalar NMP choosing $m^*/m = 0.9$ to meet the GQR and $K = 234$ MeV

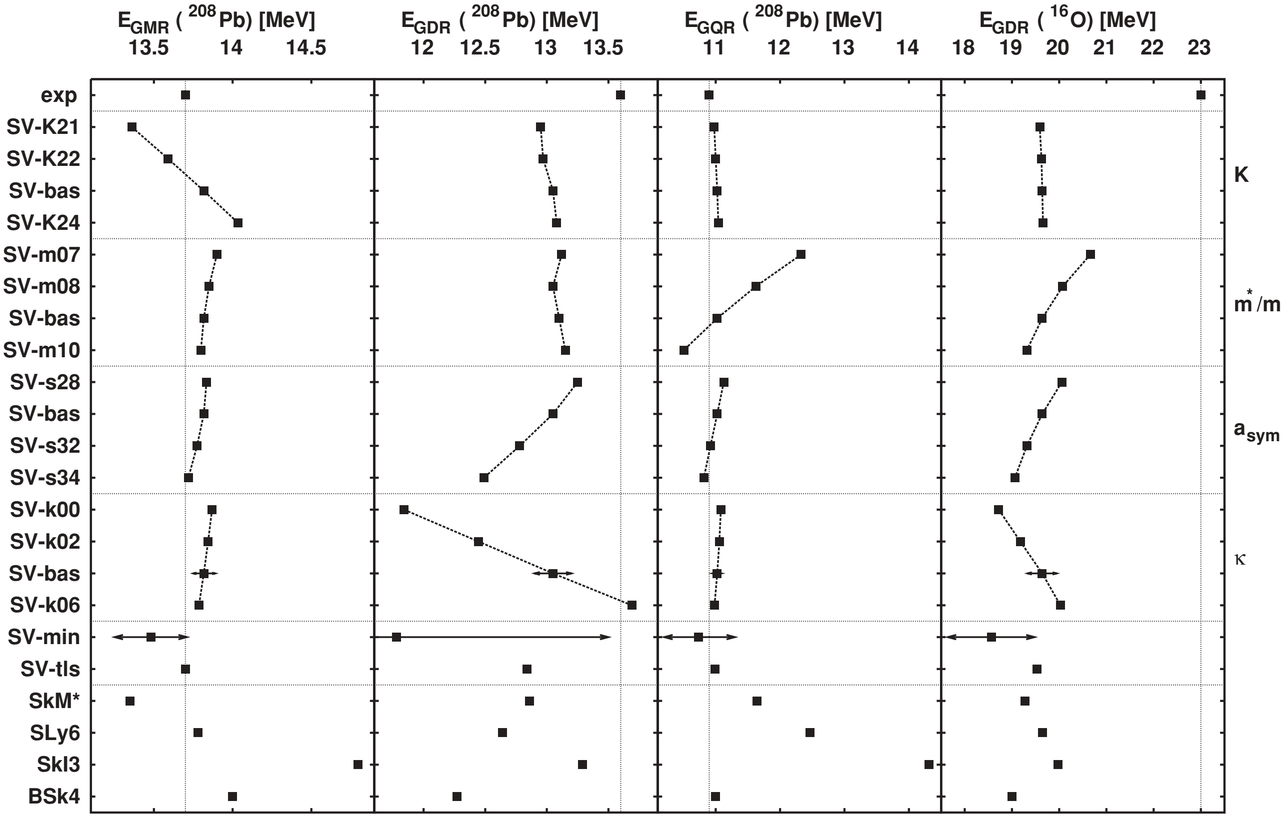

FIG. 6. Mean resonance frequencies for giant resonances in ^{208}Pb (from left to right: GMR, GDR, and GQR) and for the GDR in ^{16}O computed with the various forces encompassing systematic variation of NMP properties incompressibility K, effective mass m^*/m, symmetry energy a_{sym}, and sum-rule enhancement κ as indicated at the right side of the panels. Additionally, results from SV-min, SV-tls, and traditional Skyrme forces, as indicated, comprise the lower entries. Extrapolation errors for the three observables are shown as error bars for SV-bas and SV-min. Those for SV-bas apply to all forces fitted with constrained NMP. The experimental values are given in the uppermost entry and drawn through as faint vertical lines.

to tune the GMR. The case is much more involved for the isovector GDR that reacts to two isovector NMP, to a_{sym} and to κ. Moreover, the spectral distribution (not shown here) tends to be strongly fragmented, particularly for high m^*/m and high κ. Lower m^*/m are excluded because we want to maintain the good adjustment of the GQR. Thus we stay with a compromise for the GDR, choosing $\kappa = 0.4$ and $a_{\mathrm{sym}} = 30$ MeV. This obviously does not perfectly meet the experimental peak position for the GDR. But the example of the GDR in ^{16}O discussed later on demonstrates that the description of GDR by SHF is anyway not yet well under control. The compromise here is to be understood as a preliminary setting, open for the necessary further studies on the GDR. Fixing these four settings in the fit yields the force SV-bas as introduced in the previous section. It serves as base point for further variations of NMP. The extrapolation uncertainties for SV-bas are, of course, much smaller than those for SV-min because the uncertainty in NMP has been fixed by choice. The strong reduction of the uncertainties confirms once more the close relation between GR and NMP.

The force SV-tls is fitted as SV-bas, but with the tensor spin-orbit term switched on. There are only small changes as compared to SV-bas. These subtle shell effects seem to have an only secondary influence on GR.

The four lowest entries of Fig. 6 shows results from a few conventionally used Skyrme forces. The variation of the predictions is large, confirming once more that GR are only loosely determined by ground-state fits and that explicit adjustment is needed for satisfying performance. Again, the GDR is not well described by any one of the four traditional forces. That does also hold for the force SGII that was developed originally for GR [61] and for which we obtain the GDR peak at 12.6 MeV, well within the results from other forces.

2. *GDR in the light nucleus* ^{16}O

The rightmost column in Fig. 6 collects results for the peak position of the GDR in ^{16}O. Three of the four NMP show strong effects (κ, m^*/m, and a_{sym}). The isovector chains along a_{sym} and κ show the same trends that are at first glance natural in that the $E_{\mathrm{GDR}}(^{16}\mathrm{O})$ peak moves up with increasing $E_{\mathrm{GDR}}(^{208}\mathrm{Pb})$. The sensitivity to variation of m^*/m that is not present in ^{208}Pb shows that the GDR in ^{16}O is more sensitive to shell effects than in ^{208}Pb. But these are all comparatively moderate effects. The comparison with the average experimental peak reveals a disaster. All results stay far below the goal. We have checked all conceivable variations within the energy-density functional (3), in earlier investigations [62] and in the course of the present survey, and found no way to come approximately close to the experimental $E_{\mathrm{GDR}}(^{16}\mathrm{O})$ without dramatic sacrifices on the quality of the ground-state description. Note that also none of the conventional Skyrme forces are able to reach approximately the wanted peak frequency. We conclude that there is no way to achieve a satisfying description of the GDR throughout all nuclei with the functional (3). There is an urgent need for a thorough investigation of that case.

D. Fixing open options of the model

The SHF functional (3) leaves a few options open concerning the spin-orbit model and the pairing functional. It is worth checkind whether the χ^2 measure can help deciding about preferred choices. To that end, we start from SV-bas and vary each one of these options separately. That variation proceeds similar to the variation of NMP. We fix the selected parameter at a wanted value and refit the other force parameters again by minimization of χ^2 with additionally constraining the NMP to the values as used in SV-bas. We so to say produce variants of SV-bas with one more parameter (either ρ_{pair} or $\eta_{\mathrm{tensor-ls}}$ or b_4') fixed.

1. *Pairing model: DI versus DDDI*

Figure 7 shows the χ^2 for variation of the cutoff density ρ_{pair} in the DDDI functional (3e). The results are drawn versus $\rho_{\mathrm{pair}}^{-1}$ because that provides a better scale. The limits are as follows: $\rho_{\mathrm{pair}}^{-1} \longrightarrow 0$ leads back to DI while $\rho_{\mathrm{pair}}^{-1} = 0.16^{-1}\,\mathrm{fm}^3 = 6.25\,\mathrm{fm}^3$ is the typical DDDI value. The minimum χ^2 obviously lies between these two limits and the gain is considerable. We thus decide to use ρ_{pair} as a free parameter of the pairing model.

2. *The tensor spin-orbit term*

The spin-orbit model leaves the option of including the tensor term $\propto \mathbf{J}^2$ stemming from the kinetic interaction. Many parametrizations ignore that term. A recent compilation explored the impact of tensor spin-orbit with flexible weight [63] without finding clear signatures for optimum values. We have introduced a continuous switch factor η_{tls} to allow inclusion as tunable parameter. Figure 8 shows the result of a variation of η_{tls}. There is a steep increase in χ^2 from $\eta_{\mathrm{tls}} = 0$ to $\eta_{\mathrm{tls}} = 1$ and an almost flat landscape extending toward moderately negative values of η_{tls}. The extremely shallow χ^2 landscape will make fits extremely cumbersome because there is no drive to a clear minimum and negative values for the tensor switch factor seem a bit unorthodox. We thus decide to freeze the option $\eta_{\mathrm{tls}} = 0$, i.e., omitting tensor spin-orbit, and to consider $\eta_{\mathrm{tls}} = 1$ (= full tensor spin-orbit) occasionally as a separate option.

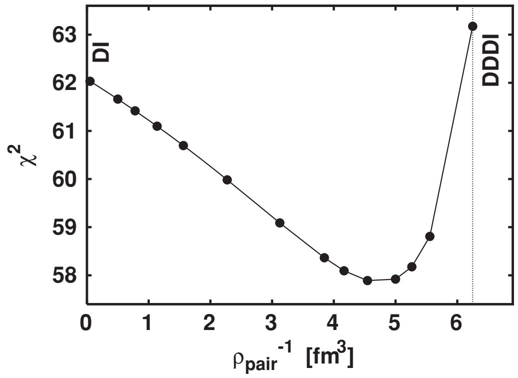

FIG. 7. Total quality measure χ^2 as function of the inverse density-switching parameter $\rho_{\mathrm{pair}}^{-1}$ in the variable DDDI functional. The DI limit relates to $\rho_{\mathrm{pair}}^{-1} = 0$. The standard DDDI parameter $\rho_{\mathrm{pair}} = 0.16\,\mathrm{fm}^{-3}$ is indicated by a vertical dotted line.

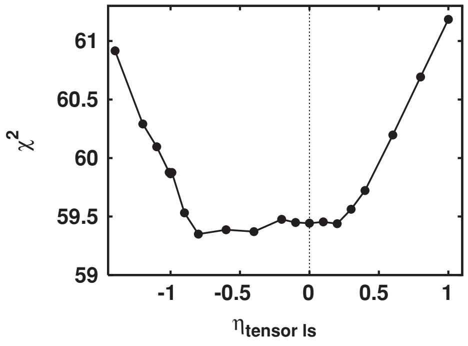

FIG. 8. Total quality measure χ^2 as function of the tensor-spin-orbit factor $\eta_{\mathrm{tensor-ls}}$. The value $\eta_{\mathrm{tensor-ls}} = 0$ (indicated by a vertical dotted line) is associated with ignoring tensor l*s coupling and $\eta_{\mathrm{tensor-ls}} = 1$ with the full term as derived from a zero-range kinetic interaction.

3. *Isovector spin-orbit term*

The other open point concerns isovector spin-orbit coupling. That is described by the parameter b_4' in the Skyrme functional (3a). A fixed isovector fraction with $b_4' = t_4/2$ is the standard spin-orbit model in conventional SHF functionals. A nonrelativistic limit from the RMF suggests $b_4' \approx 0$ as the appropriate choice [25,64]. Figure 9 shows the χ^2 as function of the ratio $2b_4'/t_4$. A value of zero corresponds to the RMF

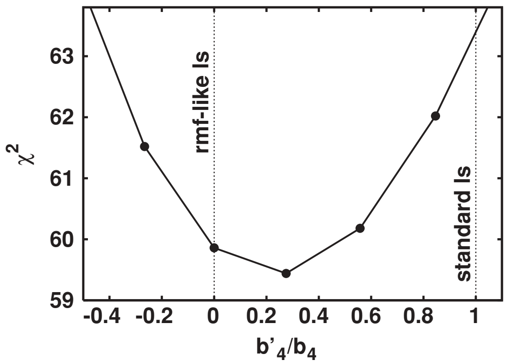

FIG. 9. Dependence of the total quality measure χ^2 on the ratio between isovector l*s coupling b_4' and isoscalar l*s coupling $b_4 = t_4/2$.

preference and one to the standard spin-orbit model of SHF. There is a considerable sensitivity. The minimum comes close to the RMF situation for the present test cases. However, the optimal b_4'/b_4 depends somewhat on the NMP constraints (e.g., effective mass, sum-rule enhancement), as seen in Table V. We thus decide to consider b_4' as a freely fitted parameter of the model.

E. Performance for other observables

In the following, we will explore the effect of variation of NMP on various detailed observables. It often happens that only one NMP shows significant effects on a given observable. In such a case, we will show only the one most relevant variation.

1. Neutron skin in ^{208}Pb

A conceptually simple observable is the neutron radius. It complements the radius information gained from the charge form factor. Unfortunately, its experimental determination is model dependent because the strong interaction is involved [66]. With that precaution, we consider the neutron radius in ^{208}Pb from Ref. [65]. We express it as neutron skin, i.e., as difference between neutron and proton radius and take as experimental reference value $r_n - r_p = 0.15$ fm. The neutron skin turns out to depend exclusively on the symmetry energy a_{sym} while all other NMP have no effect at all. The trend is shown in Fig. 10. One may even add a result from any other force into that plot and all would line up nicely on the given slope [16,62]. The minimal fit SV-min agrees with the data within the extrapolation error. However, one has to take into account that the experimental neutron radius is extracted employing model analysis of data [65]. Some uncertainty is associated with that result. We have adopted an experimental uncertainty of 0.05 fm, which still leaves a huge degree of freedom for a_{sym}. Only the conventional RMF parametrizations with their rather large $a_{\mathrm{sym}} > 34$ MeV can safely be excluded [16]. It is highly desirable to have more reliable data for the neutron skin in heavy, neutron-rich, nuclei. That would provide direct access to the symmetry energy.

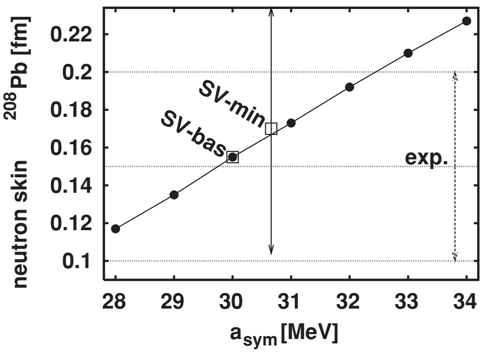

FIG. 10. The neutron skin, $r_p - r_n$, in ^{208}Pb as computed by the parametrizations with varied symmetry energy a_{sym}. The experimental value from Ref. [65] is drawn as a faint horizontal line together with assumed errors of ±0.05 fm. The set SV-min is shown together with the extrapolation errors. The extrapolation errors for SV-bas are smaller than the symbol.

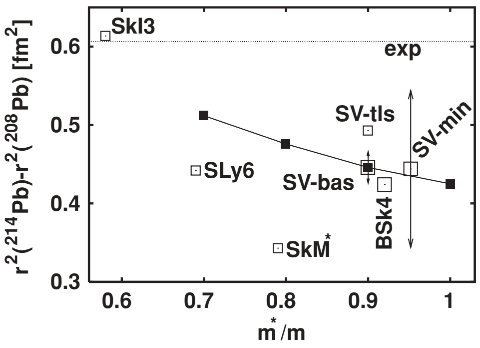

FIG. 11. The isotopic shift, $r^2(^{214}\mathrm{Pb}) - r^2(^{208}\mathrm{Pb})$, of charge radii as computed by the parametrizations with varied effective mass m^*/m (full squares). The experimental value is drawn as faint horizontal line [67]. Results from some standard parametrizations are drawn as open squares and labeled with their names in the literature. The parametrization SV-tls is a new fit with constraints as SV-bas, but using the full tensor spin-orbit, i.e., $\eta_{\mathrm{tls}} = 1$, see the SHF functional (3a). Extrapolation errors are indicated by arrows for SV-bas and SV-min.

2. The isotope shift from ^{208}Pb *to* ^{214}Pb

Another observable related to nuclear shape is provided by the isotope shifts of charge radii. These are well accessible by optical methods [67] and differences of radii put weight on aspects complementing information from radii as such. Particularly interesting here is the shift $r^2(^{214}\mathrm{Pb}) - r^2(^{208}\mathrm{Pb})$ that is usually not well described in SHF with the traditional form for the spin-orbit term but very well in RMF [25,68]. We will look at that observable with respect to the experimental result $r^2(^{214}\mathrm{Pb}) - r^2(^{208}\mathrm{Pb}) = 0.6085\,\mathrm{fm}^2$ [67]. Figure 11 collects results for that isotope shift. From the four NMP, m^*/m shows the strongest effect, although the other NMP are not totally ignorable, the forces with varying K yield a variation of 0.02 fm^2, a_{sym} spans 0.05 fm^2, and κ 0.03 fm^2. All these variations stay a factor of two below the strongest one for m^*/m. The non-negligible extrapolation error of SV-bas indicates that there are also other ingredients of the force that influence the isotopic shift. The isovector spin-orbit force does so by construction [25] and the density dependence of the pairing force is supposed to also have some effect [69]. The difference between SV-tls and SV-bas indicates the large impact of tensor spin-orbit. The present study using systematic variation of NMP, however, reveals that the effective mass still has the leading influence. It was the low m^*/m of the older generation of forces that enhanced the impact of the isovector spin-orbit term with b_4' such that it lead to the success of SkI3 and SkI4 in adjusting the isotopic shift [25]. The present preference for a higher effective mass leaves no chance to reproduce the isotope shift equally well. This becomes obvious from the errorbars of SV-min and calls for new investigations on that subject.

3. Neutron level sequence in ^{132}Sn

The single-particle energies are a subtle observable in connection with mean-field models. Density functional theory does not give a guarantee that they are correctly described [13]

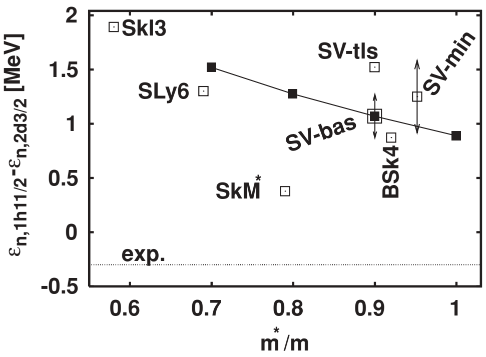

FIG. 12. The energy difference between two occupied neutron levels near the Fermi surface in ^{132}Sn, $\varepsilon_{n,1h11/2} - \varepsilon_{n,2d3/2}$, for the chain of varying effective mass and some other Skyrme parametrizations as indicated. The experimental value is indicated by a faint horizontal line [70]. Extrapolation errors are indicated by arrows for SV-bas and SV-min.

and indeed they are hampered by the self-interaction error. That error, however, leaves the energy differences untouched [71]. The robustness of single-particle energy differences has also been confirmed in the nuclear context [45,46]. Moreover, the detailed level structure plays a crucial role for the properties of SHE [72]. It is thus important to investigate the performance of mean-field models in that respect. Simple test cases can be only doubly magic nuclei to avoid perturbations from pairing and polarization effects. The levels are usually described fairly well in ^{208}Pb to the extent that at least the level ordering is usually correctly reproduced and often also the detailed energy differences [4]. However, a particularly obnoxious case is the sequence of occupied neutron levels in ^{132}Sn. The experimental ground state of ^{131}Sn has a spin $3/2^+$ while all mean-field models predict $11/2^-$ spin. We take the energy difference between these two states, $\varepsilon_{\mathrm{n,1h11/2}} - \varepsilon_{\mathrm{n,2d3/2}}$, as one number characterizing the sequence. Figure 12 shows the results for the chain with varied m^*/m. It is not surprising that this variation has most effect because m^*/m is closely related to shell structure. The next sensitive NMP is κ (not shown here) that is related to the isovector effective mass. The other parametrizations in the figure gather between 1 and 2 MeV and all theoretical results (including those from the RMF [4,45]) are far off the experimental value.

The origin of this discrepancy is not clear. It may be related to a peculiarity of the high angular momentum state involved in that difference, either that its spin-orbit splitting is underestimated or that the mean position of high spatial angular momenta is too high. It would require extensions of the SHF functional to cure one of these two features. But it could also be a problem with the interpretation of the excitation spectrum in ^{131}Sn as neutron levels in ^{132}Sn. What has not yet been checked so far is the influence of particle-core coupling in ^{132}Sn. The problem of the level sequence calls for further thorough investigations.

A similar discrepancy is seen for the energy difference between the proton $1h11/2$ and $2g7/2$ levels in Sn isotopes [73] where all mean-field models yet fail to reproduce the isotopic trend of the splitting. Two states with high angular momentum are involved. This suggests that an insufficient description of spin-orbit splitting is the more likely source of trouble. But again, this has yet to be investigated in more detail.

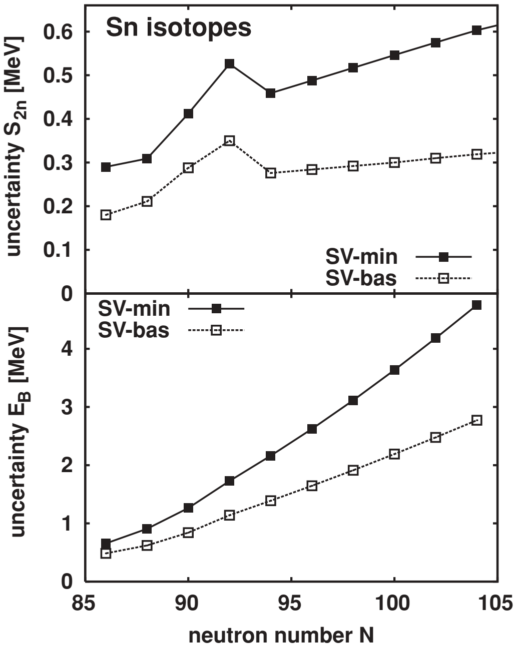

FIG. 13. Performance for extrapolations to extremely neutron-rich Sn isotopes for the two parametrizations SV-min and SV-bas. (Lower panel) Predicted extrapolation uncertainties for binding energies. (Upper panel) Predicted extrapolation uncertainties for two-neutron separation energies S_{2n}.

4. *Extrapolations to neutron-rich* Sn *Isotopes*

Astrophysical applications for *r*-process nuclei involve extrapolations deep into the regime of neutron-rich isotopes. Figure 13 shows the extrapolation errors as estimated from the least-squares techniques for binding energies and two-neutron separation energies along the chain of exotic Sn isotopes. The lower panel for binding energies shows a systematic growth of the uncertainty when moving away from the valley of stability. Note that the freezing of crucial NMP by tuning of giant resonances in SV-bas reduces the uncertainty by a factor of two. The upper panel for two-neutron separation energies basically behaves similarly, but the errors are much smaller than for the energies as such. Differences of energies probe the response properties and these are obviously a bit more robust. Note also the peak at neutron number $N = 92$. There is a small subshell closure that is particularly sensitive to shell structure. The increase of uncertainty here indicates that an aspect of shell structure comes into play that is not so well determined as the general trends.

5. *Fission barriers in* ^{236}U

Fission of actinides is a crucial nuclear reaction that serves as a sensitive probe for many aspects of nuclear structure, depending on macroscopic properties as well as on the nuclear level density [4,55]. We use it here as a further critical observable for tesing Skyrme parametrizations. Fission is usually characterized in terms of fission barriers. We deduce the barriers from quadrupole-constrained SHF calculations considering axially symmetric shapes and allowing for reflection asymmetry. A series of constrained calculations for a broad range of deformations spans the fission path and the associated deformation energy surface. All states along the path are well deformed. We thus compute the energy with the correction from angular-momentum projection in GOA, as explained in Sec. II. That energy curve for actinides displays the typical double-humped barrier [74] with one isomeric minimum. From that we read off two barrier heights and the isomeric energy. It is to be noted that the first barrier tends to go through triaxial shapes, not accounted for here. A further lowering by 0.5–2 MeV can be expected from triaxiality [76,77].

Figure 14 shows results for fission isomer and fission barrier for ^{236}U as a typical example for an actinide. The values fit generally well to the experimental data, particularly when considering some triaxial lowering for the first barrier. The strongest influence from NMP on the first barrier comes from the symmetry energy a_{sym}, some effect is added from m^*/m, and K as well as κ remain basically inert. The order is reversed for the second barrier where m^*/m has largest impact and a_{sym} is secondary. These two NMP are the crucial handles on fission properties including the isomer. This reflects that fission emerges from a subtle interplay of bulk properties (here a_{sym}) and shell effects (here m^*/m). The impact of shell effects through the spin-orbit force is seen also in the step from SV-bas to SV-tls that yields a small, but non-negligible, lowering of the barriers.

It is interesting to note that the variation of results for the conventional forces is larger than the variation within all SV forces. That indicates a large sensitivity of fission properties to fitting strategies.

6. A known SHE: ^{264}Hs

Some SHE have already been produced such that data are available for probing the predictive power directly. We consider here ^{264}Hs as sample. The nucleus has a well-deformed ground state. In fact, it belongs to an island of deformed shell closures [76,80]. We discussed it, among others, already in connection with Figs. 3 and 4. Here, we continue with more detailed variations. Figure 15 shows the

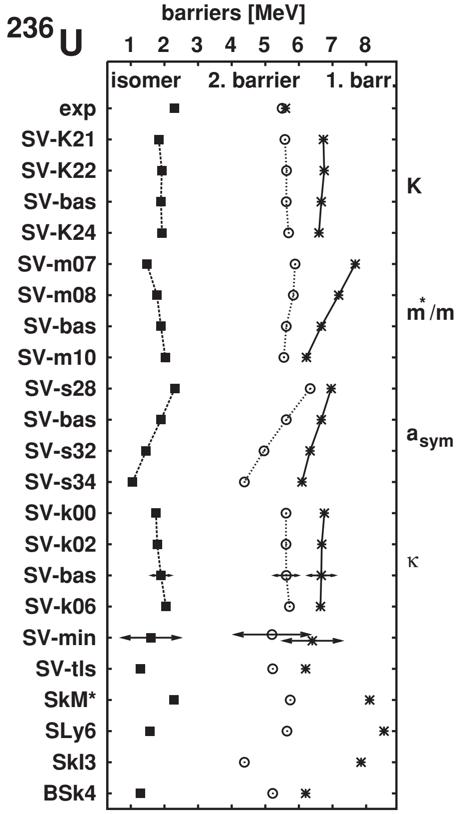

FIG. 14. Axially symmetric fission barriers (star = first barrier, open circle = second barrier) and position of the isomeric minimum (filled square) in ^{236}U for the variety of parametrizations as indicated. The first barrier extrapolation errors are shown for SV-bas and SV-min. The errors for SV-bas are representative for all forces with constrained NMP. The experimental values are taken from Refs. [74, 75].

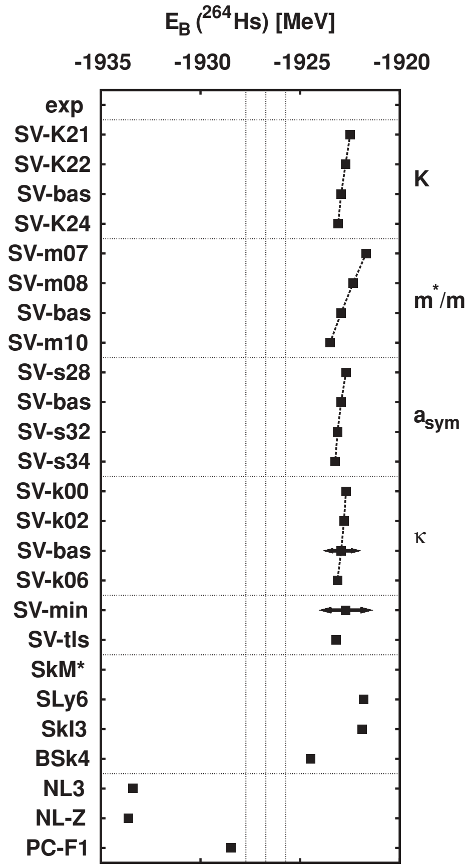

FIG. 15. The binding energy of ^{264}Hs for the variety of parametrizations as indicated. The lowest three entries show results from relativistic mean-field models [78,79]. Extrapolation errors are shown for SV-bas and SV-min. The errors for SV-bas are representative for all forces with constrained NMP.

binding energy of ^{264}Hs for all forces in our sample. The test case embraces extrapolation to SHE together with deformation effects. It is thus very sensitive and we find that all NMP have some influence, the strongest coming from m^*/m. But none of the allowed variations of NMP brings the result in any way close to the experimental value. The same holds true for the conventional Skyrme forces. That feature was already observed in Ref. [78] and it was also found that relativistic mean-field models behave quite differently. Thus we have added a few results from relativistic models, NL-Z [81], NL3 [82], and PC-F1 [79]. These tend to overbinding where SHF generally yields underbinding. The result indicates a deep-rooted structural difference between these two classes of models and possibly missing terms in both.

Reactions in the landscape of SHE are not so much determined by binding energies as such. Differences of binding energies are more crucial, particularly the Q_α value that characterizes α decay. Figure 16 shows Q_α for ^{264}Hs in comparison to the experimental value. All forces provide rather nice agreement with the experimental value. There is general trend to about 0.2 MeV underestimation. This may be due to the fact that the daughter nucleus $Z = 106$ is softer than the parent $Z = 108$ such that some additional correlation effect may come into play. Nevertheless, the agreement is much better than what one could have expected from the variations in the binding energies (see Fig. 15). That indicates that energy differences can be predicted more safely.

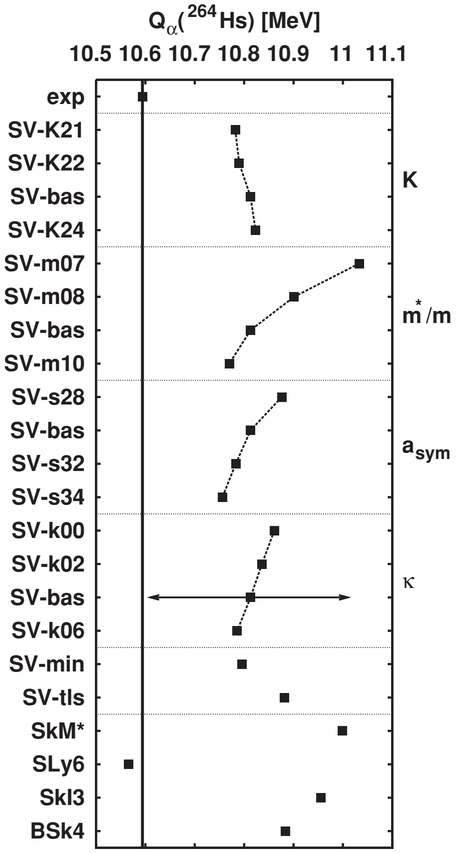

FIG. 16. The Q_α value of ^{264}Hs for the variety of parametrizations as indicated. Extrapolation errors are shown for SV-bas. Those for SV-min exceed the bounds of the plot.

7. At the upper end a spherical SHE: $Z, N = (120, 182)$

Further up, there are very interesting, yet unmeasured, SHE. In that regime, we consider as test case element $Z, N = (120, 182)$, at the upper edge of experimental feasibility in the regime of the spherical valley of stability. It resides on an upward extension of an α-decay chain recently detected [83–85]. This is a spherical nucleus due to the proton shell closure at $Z = 120$ and a a low-level density for the neutrons at their Fermi energy [86–88]. We consider for that element the binding energy E_B as such, the Q_α value

$$Q_\alpha(Z, N) = E_B(Z-2, N-2) + E_B(2, 2) - E_B(Z, N), \quad (15)$$

which characterizes α decay and the fission barrier B_{fis}. The latter quantity is deduced from computing the potential-energy surface along the axially symmetric quadrupole deformation path, for details see Ref. [89], including again the correction from angular-momentum projection. Most SHE have only a single fission barrier.

Figure 17 shows the results for the hypothetical nucleus $(Z/N) = (120/182)$. We concentrate first on the binding energy (left column). The span of predictions from conventional parametrizations is huge. The force SkM* is far off all other results that could be explained by two reasons: First, it is the oldest force in the sample and it was adjusted on a smaller data base available at that time [55]. Second, and probably more important, SkM* is the only force in the sample that uses a different recipe for the center-of-mass correction, namely to take only the diagonal elements of the $\hat{P}_{\text{cm}}$ in Eq. (3f) that has dramatic consequences for the extrapolation to SHE [90]. The more recent forces are grouped somewhat better together, and the whole set of SV forces shows comparatively little variation. The extrapolation error of SV-min is still smaller than the difference to conventional forces and SV-bas comes down to an uncertainty of ±0.8 MeV. The difference in the extrapolation errors between SV-min and SV-bas shows the influence of the loosely fixed NMP. A better determination of NMP through GR does also improve the predictive value in the regime of exotic nuclei. The right column of Fig. 17 shows the fission barriers for the SHE 120/182. These are sensitive to all details of a parametrization due to the subtle interplay of bulk properties (surface tension, Coulomb pressure) and shell effects. All NMP yield 1–2 MeV variation of the result. The sizable extrapolation errors of about 0.8 MeV for SV-bas show that there are other effects also at work. The fission barrier is determined by bulk properties (i.e., NMP) as well as shell effects [89]. The latter can be seen, e.g., by the large effect of the tensor spin-orbit force, see the difference between SV-bas and SV-tls. In spite of all these sensitivities, the more conservative extrapolation error of SV-min indicates that the predictions can be taken within about 1.2 MeV reliability. It is comforting to see that most of the conventional parametrizations stay also within these bounds. Thus we see that SHF notoriously predicts the fission barrier for 120/182 around 6 MeV with angular-momentum correction

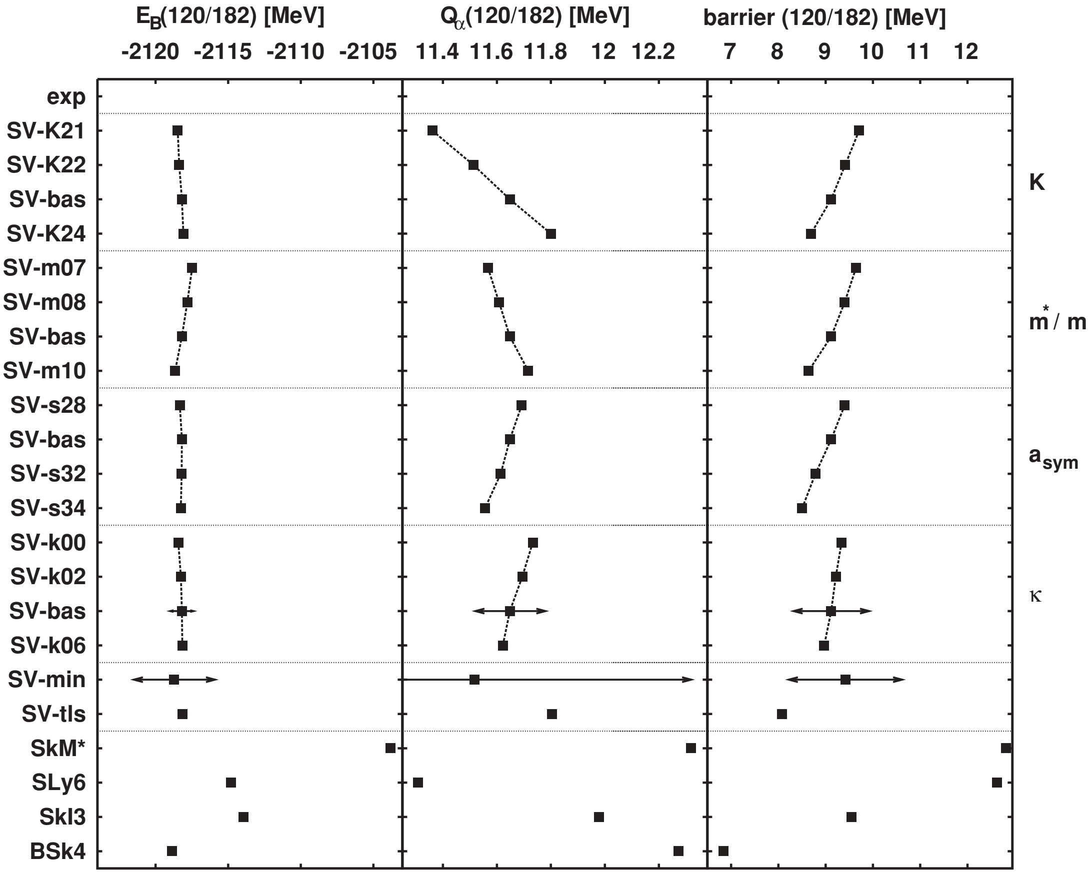

FIG. 17. Results of the various forces for the super-heavy element $(Z/N) = (120/182)$. (Left column) Total binding energy. (Middle column) Q_α value. (Right column) Fission barrier. Extrapolation errors are shown for SV-bas and SV-min. The errors for SV-bas are representative for all forces with constrained NMP.

and 7–8 MeV without. That remains in great contrast to the RMF where all predictions come out much lower [89].

There is a competition between α decay and fission in the decay channels of SHE. The middle column of Fig. 17 shows the Q_α value for the SHE 120/182. This quantity is directly deduced from a difference of binding energies. One would expect similar trends as for the binding energies (left column), but differences can suppress one trend and amplify another. That is what happens for the Q_α. The trend with m^*/m looses importance and the incompressibility K acquires more weight, but the variations are generally much smaller than for the fission barriers. Except for SkM*, all forces agree within ±0.4 MeV. The fact that the extrapolation error for SV-bas is much smaller than for SV-min indicates that NMP are the leading determinators, in contrast to fission barriers where shell effects have much larger influence.

V. CONCLUSION

In this article, we have performed a survey of the phenomenological adjustment of the free parameters of the SHF energy functional. The input data for the fits are taken from basic nuclear ground-state properties: energies, charge radii, surface thickness, selected odd-even staggering of energies, and some spin-orbit splittings. These data and appropriate nuclei are selected carefully such that they have small correlation effects. Thereby we consider only the strongly fluctuating correlations from low-lying collective quadrupole states. The smoothly varying correlations from higher excitations (two-body collisions and resonances) are supposed to be incorporated effectively in the SHF functional. The investigation of correlation effects led to a selection of semimagic fit nuclei with large extension along isotonic chains but surprisingly short isotopic chains. All selected nuclei are spherical to avoid ambiguities from the handling of deformed minima (angular-momentum projection). A quality measure χ^2 is built from summing the squared deviations from the data with appropriate adopted error weights. The parameters of the SHF functional are optimized by least-squares fits with respect to the selected sample of data. The emerging r.m.s. errors in the fit observables stay well (by a factor two) below the adopted input errors from correlation effects that shows that the SHF model has some flexibility to incorporate part of correlations from the low-lying excitations. It is found that the χ^2 minimization leaves some freedom in nuclear bulk properties. To explore the space of well-fitted forces thus becoming available, we have performed a systematic variation of bulk properties, characterized in terms of NMP. This is achieved by adding to the selected ground-state data constraints on four NMP: incompressibility K, effective mass m^*/m, symmetry energy a_{sym}, and sum-rule enhancement factor κ. These NMP are varied systematically to produce a set of forces with different properties, all having about the same high quality concerning the nuclear ground-state properties in the fit data. The set of parametrizations thus obtained was used for a thorough investigation of the predictive power of the SHF model by looking at the results for several detailed observables in stable and super-heavy nuclei.

We have used the quality measure χ^2 to check some open options of the present ansatz for the SHF functional. There used to be the decision between volume pairing that corresponds to a simple zero-range pairing force and surface pairing that augments that with a density dependence such that pairing is basically switched off for densities near bulk equilibrium. We have allowed a flexible switching with a density parameter between bulk equilibrium (surface pairing) and infinity (volume pairing). It turns out that the optimum choice is just between these extremes. The SHF functional allows a free choice for the isovector spin-orbit force. A free variation is found to be advantageous as compared to the standard choice that is linked to the isoscalar value or to the choice of zero isovector term deduced from the RMF. There is, furthermore, the choice to include the tensor spin-orbit term that is related to the kinetic zero-range two-body interaction. The quality measure prefers a model without tensor spin-orbit. All three decisions, however, are related to changes in the total χ^2 by about 5%.

We have looked at the separate contributions of an observable (e.g., energy) to the total χ^2. The trends of these contributions with systematically varied NMP pull often in different directions. This means that the choice of relative weights of one observable with respect to another decides on the final result. The trends are weak and thus small changes in weight can cause large drifts in final NMP of a least-squares minimum. This is a quite undesirable element of arbitrariness in the adjustment procedure. However, the weakness of the trends means that there are several features not so sharply determined from ground-state fits. We exploit the freedom to additionally adjust the peak positions of three decisive giant resonances in ^{208}Pb: the isoscalar GMR, the isoscalar GQR, and the isovector GDR. The GMR fixes the incompressibility and the GQR the effective mass. Both resonances can be well described by the model. The GDR is less conclusive in two respects. First, it is sensitive to two NMP, the symmetry energy and the sum-rule enhancement factor. And second, it does not yet allow fully satisfying tuning due to the strong fragmentation pattern. Moreover, we find that the GDR in ^{16}O is far off the experimental peak position for all reasonable SHF parametrizations. The present forms of the SHF functional do not yet allow a proper description of the GDR throughout all nuclei. This case of the GDR still requires further investigation.

In summary, we have built one force, SV-min, with minimal χ^2 from an unrestricted fit, another force, SV-bas, from NMP-constrained fits with GR fine-tuning, a series of forces with systematically varied NMP, and finally a variant of SV-bas with a tensor spin-orbit term. Using this set of trial forces, we have investigated the performance for other nuclei and the predictions for a variety of more detailed observables. The interpolation to nuclei within the fitted mass range, i.e., $A < 220$, perform fairly well when including angular-momentum projection. The remaining underbinding of 1–2 MeV for soft nuclei is resolved by vibrational correlations. The extrapolation to heavier, deformed nuclei, however, develops large underbinding up to 4 MeV. The attempt to cure that by including super-heavy elements in the fit did not work out well. It sacrifices too much of the quality reached for stable nuclei. We encounter here most probably a problem with an insufficient form of the present energy functional. The binding energy of spherical super-heavy nuclei is a rather robust quantity depending mainly on the effective mass and other features influencing shell structure. Deformed super-heavy nuclei are more sensitive because of the deformation energy. The fission barriers in super-heavy elements is more sensitive depending on almost any feature of the force, all NMP and more detailed entries as, e.g., the tensor spin-orbit term. Nonetheless, all predictions lie within a band of ±1.2 MeV of about 10 MeV, which is a very comforting result for such a subtle observable. Even more robust are the Q_α energies determining the rate of α decay, which are most strongly influenced by the incompressibility. This shows that differences of energies can behave differently from the energies as such (where the effective mass was most influential). The neutron skin in ^{208}Pb depends exclusively on the symmetry energy. It would be the ideal means to determine this crucial isovector property, but the measurement needs to be reliable and precise. An uncertainty of 0.02 fm in the neutron radius translates to an uncertainty of 1 MeV in the symmetry energy. Practically all existing SHF parametrizations comply with the presently available data within their large uncertainties. The isotope shift of charge radii between ^{214}Pb and ^{208}Pb depends sensitively on the effective mass and other features influencing the shell structure. The recent fits all tend to rather large effective mass that, in turn, raises problems with accommodating that isotopic shift, even when allowing full freedom in the isovector spin-orbit term. The case, which seemed to be solved for previous parametrizations with low effective mass, is open again and requires further investigations.

Altogether, we find that the SHF model provides an excellent description of nuclear bulk properties. Ground-state properties alone, however, leave several features weakly determined. Additional information from excitation or more detailed ground-state observables is required to fix all aspects of the SHF model. At the same time, the added observables reveal some insufficiencies of the model that call for further investigations. Most urgent seems to be an extension of the spin-orbit model and a better description of dipole giant resonances.

ACKNOWLEDGMENTS

This work was supported by BMBF under Contract Nos. 06 FY 159D and 06 ER 142D. We gratefully acknowledge support by the Regional Computing Center Erlangen.

APPENDIX: DETAILS ON DATA AND PARAMETERS

TABLE III. Experimental data for the fits, part I: along isotopic chains. Each column stands for an observable as indicated. The second line shows the globally adopted error for each observable. That error is multiplied for each observable by a further integer weight factor that is given in the column next to the data value.

A	Z	E_B (±1 MeV)		R_{diffr} (±0.04 fm)		σ (±0.04 fm)		r_{rms} (±0.02 fm)		$\varepsilon_{ls,p}$ (±20%)		$\varepsilon_{ls,n}$ (±20%)		Δ_p (±0.12 MeV)		Δ_n (±0.12 MeV)	
16	8	−127.620	4	2.777	2	0.839	2	2.701	2	6.30	3	6.10	3				
36	20	−281.360	2														
38	20	−313.122	2														
40	20	−342.051	3	3.845	1	0.978	1	3.478	1								
42	20	−361.895	2	3.876	1	0.999	1	3.513	2							1.68	4
44	20	−380.960	2	3.912	1	0.975	1	3.523	2							1.70	2
46	20	−398.769	2					3.502	1							1.49	4
48	20	−415.990	1	3.964	1	0.881	1	3.479	2								
50	20	−427.491	1					3.523	9								
52	20	−436.571	1														
56	28	−483.990	5					3.750	9								
58	28	−506.500	5	4.364	1			3.776	5								
60	28	−526.842	5	4.396	1	0.926	5	3.818	5								
62	28	−545.258	5	4.438	1	0.937	5	3.848	5								
64	28	−561.755	5	4.486	1	0.916	2	3.868	5								
68	28	−590.430	1														
100	50	−825.800	2														
108	50							4.563	2								
112	50			5.477	3	0.963	9	4.596	9							1.41	9
114	50			5.509	3	0.948	9	4.610	9							1.26	9
116	50			5.541	3	0.945	9	4.626	9							1.21	9
118	50			5.571	2	0.931	2	4.640	1							1.34	9
120	50			5.591	1		1	4.652	1							1.39	9
122	50	−1035.530	3	5.628	1	0.895	1	4.663	1							1.37	3
124	50	−1050.000	3	5.640	1	0.908	1	4.674	1							1.31	3
126	50	−1063.890	2													1.26	2
128	50	−1077.350	2													1.22	2
130	50	−1090.400	1													1.17	3
132	50	−1102.900	1							1.35	1	1.65	1				
134	50	−1109.080	1														
198	82	−1560.020	9					5.450	2								
200	82	−1576.370	9					5.459	1								
202	82	−1592.203	9					5.474	1								
204	82	−1607.521	2	6.749	1	0.918	1	5.483	1							0.77	2
206	82	−1622.340	1	6.766	1	0.921	1	5.494	1							0.59	3
208	82	−1636.446	1	6.776	1	0.913	1	5.504	1	1.42	1	0.90	1				
												1.77	2				
210	82	−1645.567	1					5.523	1							0.66	3
212	82	−1654.525	1					5.542	1								
214	82	−1663.299	1					5.559	1								

TABLE IV. Experimental data for the fits, part II: along isotonic chains. Doubly magic nuclei that would fit both sequences are not repeated here. For further explanations see Table III.

A	Z	E_B (±1 MeV)		R_{diffr} (±0.04 fm)		σ (±0.04 fm)		r_{rms} (±0.02 fm)		$\varepsilon_{ls,p}$ (±20%)		$\varepsilon_{ls,n}$ (±20%)		Δ_p (±0.12 MeV)		Δ_n (±0.12 MeV)	
34	14	−283.429	2											2.22	8		
36	16	−308.714	2	3.577	4	0.994	4	3.299	1					1.52	8		
38	18	−327.343	2					3.404	1					1.44	8		
42	22	−346.904	*														
50	22	−437.780	2	4.051	1	0.947	2	3.570	1								
52	24	−456.345	*	4.173	1	0.924	4	3.642	2								

TABLE IV. *(Continued.)*

A	Z	E_B ($\pm$1 MeV)		R_{diffr} ($\pm$0.04 fm)		σ ($\pm$0.04 fm)		r_{rms} ($\pm$0.02 fm)		$\varepsilon_{ls,p}$ ($\pm$20%)	$\varepsilon_{ls,n}$ ($\pm$20%)	Δ_p ($\pm$0.12 MeV)		Δ_n ($\pm$0.12 MeV)
54	26	−471.758	*	4.258	1	0.900	4	3.693	2					
84	34	−727.341	*									1.33	9	
86	36	−749.235	2					4.184	1			1.33	3	
88	38	−768.467	1	4.994	1	0.923	1	4.220	1			1.30	2	
90	40	−783.893	1	5.040	1	0.957	1	4.269	1					
92	42	−796.508	1	5.104	1	0.950	1	4.315	1			1.40	2	
94	44	−806.849	2									1.33	2	
96	46	−815.034	2											
98	48	−821.064	2											
134	52	−1123.270	1									0.81	4	
136	54	−1141.880	1					4.791	1			0.98	2	
138	56	−1158.300	1	5.868	2	0.900	2	4.834	1			1.12	2	
140	58	−1172.700	1					4.877	1			1.21	2	
142	60	−1185.150	2	5.876	3	0.989	3	4.915	1			1.23	2	
144	62	−1195.740	2					4.960	1			1.25	2	
146	64	−1204.440	2					4.984	1			1.42	2	
148	66	−1210.750	2					5.046	2			1.49	2	
150	68	−1215.330	2					5.076	2					
152	70	−1218.390	2											
206	80	−1621.060	1					5.485	1					
210	84	−1645.230	1					5.534	1			0.81	3	
212	86	−1652.510	1					5.555	1			0.88	1	
214	88	−1658.330	1					5.571	1			0.96	1	
216	90	−1662.700	1											
218	92	−1665.650	1											

TABLE V. The parameters of the energy-density functional (3) for the various SHF parametrizations used in this article. All parametrizations use a proton mass of $\hbar^2/2m_p = 20.749821$ and a neutron mass of $\hbar^2/2m_n = 20.721260$. For an explanation of the labels see Table II.

Force	t_0	t_1	t_2	t_3	t_4	$V_{\mathrm{Pair,p}}$	$V_{\mathrm{Pair,n}}$	ρ_{pair}
	x_0	x_1	x_2	x_3	b'_4	α		η_{tls}
SV-min	−2112.248	295.781	142.268	13988.567	111.291	601.160	567.191	0.21159
	0.243886	−1.434926	−2.625899	0.258070	45.93615	0.255368		0
SV-bas	−1879.639	313.749	112.677	12527.376	124.634	674.618	606.902	0.20113
	0.258546	−0.381689	−2.823638	0.123229	34.11167	0.30		0
SV-K241	−1745.184	310.497	5.705	11975.552	123.469	675.378	610.425	0.20108
	0.291787	−0.106990	−31.904438	0.157335	34.61687	0.34		0
SV-K226	−2055.773	317.043	247.652	13344.392	126.375	619.478	561.830	0.21416
	0.217498	−0.717223	−1.975946	0.081932	33.12488	0.26		0
SV-K218	−2295.822	320.278	330.798	14557.194	130.033	567.192	517.838	0.23131
	0.191803	−0.925134	−1.800814	0.068066	29.57382	0.22		0
SV-mas10	−1813.907	270.452	57.215	12965.454	127.649	665.102	588.101	0.19774
	0.232898	0.127181	−4.795203	−0.062346	27.13922	0.33		0
SV-mas08	−1982.650	368.228	274.611	12141.094	119.794	678.404	621.138	0.20781
	0.285653	−1.037404	−1.780825	0.339364	44.33569	0.26		0
SV-mas07	−2203.658	438.349	566.845	12222.736	113.522	752.655	688.246	0.20122
	0.354369	−1.782940	−1.436932	0.632534	57.76849	0.20		0
SV-sym34	−1887.367	323.804	351.782	12597.277	139.310	673.808	603.478	0.20008
	−0.230110	−0.959586	−1.775475	−0.721854	20.28327	0.30		0
SV-sym32	−1883.278	319.184	197.329	12559.469	132.745	676.730	607.540	0.19995
	0.007688	−0.594307	−2.169215	−0.309537	26.67638	0.30		0
SV-sym28	−1877.431	307.255	140.868	12511.940	115.556	590.035	539.892	0.22395
	0.517821	−0.431291	−2.474137	0.568794	42.14865	0.30		0
SV-kap06	−1880.594	314.373	194.940	12537.049	138.722	655.117	575.327	0.20717

TABLE V. *(Continued.)*

Force	t_0	t_1	t_2	t_3	t_4	$V_{\mathrm{Pair,p}}$	$V_{\mathrm{Pair,n}}$	ρ_{pair}
	x_0	x_1	x_2	x_3	b'_4	α		η_{tls}
	0.183805	0.082542	−2.161972	−0.146674	20.34984	0.30		0
SV-kap02	−1878.883	313.245	44.042	12519.929	110.511	664.612	616.996	0.20136
	0.331398	−0.879672	−5.267351	0.390236	48.25944	0.30		0
SV-kap00	−1877.891	312.600	7.104	12509.993	95.297	683.599	648.780	0.19611
	0.393391	−1.454820	−26.089659	0.640506	63.35492	0.30		0
SV-tls	−1879.892	317.952	30.265	12531.858	184.991	645.630	577.394	0.20723
	0.246413	−0.197627	−7.212765	0.103793	0.00010	0.30		1

[1] W. Nazarewicz, J. Dobaczewski, N. Michel, M. Ploszajczak, M. Stoitsov, and J. Terasaki, Nucl. Instrum. Methods B **204**, 1 (2003).

[2] W. Mittig, P. Roussel-Chomaz, and A. C. C. Villari, Eur. Phys. News **35**, 113 (2004).

[3] P. Möller, J. Nix, W. Myers, and W. Swiatecki, At. Data Nucl. Data Tables **59**, 185 (1995).

[4] M. Bender, P.-H. Heenen, and P.-G. Reinhard, Rev. Mod. Phys. **75**, 121 (2003).

[5] S. E. Koonin, D. J. Dean, and K. Langanke, Phys. Rep. **278**, 1 (1997).

[6] M. Wloch, D. J. Dean, J. R. Gour, M. Hjorth-Jensen, K. Kowalski, T. Papenbrock, and P. Piecuch, Phys. Rev. Lett. **94**, 212501 (2005).

[7] R. Roth, H. Hergert, P. Papakonstantinou, T. Neff, and H. Feldmeier, Phys. Rev. C **72**, 034002 (2005).

[8] C. Forssen, P. Navratil, W. E. Ormand, and E. Caurier, Phys. Rev. C **71**, 044312 (2005).

[9] G. F. Bertsch, J. Phys. Conf. Ser. **78**, 012005 (2007).

[10] J. Dechargé and D. Gogny, Phys. Rev. C **21**, 1568 (1980).

[11] P.-G. Reinhard, Rep. Prog. Phys. **52**, 439 (1989).

[12] P. Ring, Prog. Part. Nucl. Phys. **37**, 193 (1996).

[13] R. M. Dreizler and E. K. U. Gross, *Density Functional Theory* (Springer, Berlin, 1990).

[14] L. G. Cao, U. Lombardo, C. W. Shen, and N. V. Giai, Phys. Rev. C **73**, 014313 (2006).

[15] J. W. Negele and D. Vautherin, Phys. Rev. C **5**, 1472 (1972).

[16] J. Stone and P.-G. Reinhard, Prog. Part. Nucl. Phys. **58**, 587 (2007).

[17] M. Samyn, S. Goriely, P.-H. Heenen, J. M. Pearson, and F. Tondeur, Nucl. Phys. **A700**, 142 (2002).

[18] G. F. Bertsch, B. Sabbey, and M. Uusnakki, Phys. Rev. C **71**, 054311 (2005).

[19] M. Bender, G. F. Bertsch, and P.-H. Heenen, Phys. Rev. Lett. **94**, 102503 (2005).

[20] M. Bender, G. F. Bertsch, and P.-H. Heenen, Phys. Rev. C **73**, 034322 (2006).

[21] P. Klüpfel, P.-G. Reinhard, and J. Maruhn, Eur. Phys. J. A **37**, 343 (2008).

[22] Y. M. Engel, D. M. Brink, K. Goeke, S. J. Krieger, and D. Vautherin, Nucl. Phys. **A249**, 215 (1975).

[23] M. Bender, J. Dobaczewski, J. Engel, and W. Nazarewicz, Phys. Rev. C **65**, 054322 (2002).

[24] B. D. Serot and J. D. Walecka, Adv. Nucl. Phys. **16**, 1 (1986).

[25] P.-G. Reinhard and H. Flocard, Nucl. Phys. **A584**, 467 (1995).

[26] J. C. Slater, Phys. Rev. **81**, 385 (1951).

[27] K. W. Schmid and P.-G. Reinhard, Nucl. Phys. **A530**, 283 (1991).

[28] P. Bonche, H. Flocard, P.-H. Heenen, S. J. Krieger, and M. S. Weiss, Nucl. Phys. **A443**, 39 (1985).

[29] S. J. Krieger, P. Bonche, H. Flocard, P. Quentin, and M. S. Weiss, Nucl. Phys. **A517**, 275 (1990).

[30] M. Bender, K. Rutz, P.-G. Reinhard, and J. A. Maruhn, Eur. Phys. J. A **8**, 59 (2000).

[31] P.-G. Reinhard, Z. Phys. A **285**, 93 (1978).

[32] P.-G. Reinhard and K. Goeke, Rep. Prog. Phys. **50**, 1 (1987).

[33] P.-G. Reinhard, D. J. Dean, W. Nazarewicz, J. Dobaczewski, J. A. Maruhn, and M. R. Strayer, Phys. Rev. C **60**, 014316 (1999).

[34] K. Hagino, P.-G. Reinhard, and G. F. Bertsch, Phys. Rev. C **65**, 064320 (2002).

[35] P. R. Bevington, *Data Reduction and Error Analysis for the Physical Sciences* (McGraw-Hill, New York, 1969).

[36] J. Friedrich and P.-G. Reinhard, Phys. Rev. C **33**, 335 (1986).

[37] J. Friedrich and N. Vögler, Nucl. Phys. **A373**, 192 (1982).

[38] J. L. Friar and J. W. Negele, Adv. Nucl. Phys. **8**, 219 (1975).

[39] P.-G. Reinhard, Ann. Phys. (Leipzig) **1**, 632 (1992).

[40] P.-G. Reinhard and C. Toepffer, Int. J. Mod. Phys. E **3**, 435 (1994).

[41] J. Sauvage-Letessier, P. Quentin, and H. Flocard, Nucl. Phys. **A370**, 231 (1981).

[42] T. Duguet, P. Bonche, P.-H. Heenen, and J. Meyer, Phys. Rev. C **65**, 014311 (2001).

[43] M. Bender, T. Cornelius, G. A. Lalazissis, J. A. Maruhn, W. Nazarewicz, and P.-G. Reinhard, Eur. Phys. J. A **14**, 23 (2002).

[44] J. Dobaczewski, P. Magierski, W. Nazarewicz, W. Satuła, and Z. Szymanski, Phys. Rev. C **63**, 024308 (2001).

[45] K. Rutz, M. Bender, P.-G. Reinhard, J. A. Maruhn, and W. Greiner, Nucl. Phys. **A634**, 67 (1998).

[46] V. Bernard and Nguyen Van Giai, Nucl. Phys. **A348**, 75 (1980).

[47] W. Satuła, D. J. Dean, J. Gary, S. Mizutori, and W. Nazarewicz, Phys. Lett. **B407**, 103 (1997).

[48] P.-G. Reinhard and Y. K. Gambhir, Ann. Phys. (Leipzig) **1**, 598 (1992).

[49] P.-G. Reinhard, P. D. Stevenson, D. Almehed, J. A. Maruhn, and M. R. Strayer, Phys. Rev. E **73**, 036709 (2006).

[50] A. van der Woude, in *International Review of Nuclear Physics: Electric and Magnetic Giant Resonances in Nuclei*, edited by J. Speth (World Scientific, Singapore, 1991), Vol. 7, pp. 99–232.

[51] A. Veyssiere, H. Beil, R. Bergere, P. Carlos, and A. Lepretre, Nucl. Phys. **A159**, 561 (1970).

[52] T. C. team, cdfe.sinp.msu.ru/services (2007).

[53] J. P. Blaizot, Phys. Rep. **64**, 171 (1980).

[54] P. Ring and P. Schuck, *The Nuclear Many-Body Problem* (Springer-Verlag, New York, 1980).

[55] J. Bartel, P. Quentin, M. Brack, C. Guet, and H.-B. Håkansson, Nucl. Phys. **A386**, 79 (1982).

[56] E. Chabanat, P. Bonche, P. Haensel, J. Meyer, and R. Schaeffer, Nucl. Phys. **A635**, 231 (1998); **A643**, 441(E) (1998).

[57] S. Goriely, M. Samyn, M. Bender, and J. M. Pearson, Phys. Rev. C **68**, 054325 (2003).

[58] S. Raman, C. W. Nestor, and P. Tikkanen, At. Data Nucl. Data Tables **78**, 1 (2001).

[59] P.-G. Reinhard, M. Bender, W. Nazarewicz, and T. Vertse, Phys. Rev. C **73**, 014309 (2006).

[60] F. Osterfeld, Rev. Mod. Phys. **64**, 491 (1992).

[61] Nguyen Van Giai and H. Sagawa, Phys. Lett. **B106**, 379 (1981).

[62] P.-G. Reinhard, Nucl. Phys. **A649**, 305c (1999).

[63] T. Lesinski, M. Bender, K. Bennaceur, T. Duguet, and J. Meyer, Phys. Rev. C **76**, 014312 (2007).

[64] A. Sulaksono, P. G. Reinhard, T. J. Bürvenich, P. O. Hess, and J. A. Maruhn, Phys. Rev. Lett. **98**, 262501 (2007).

[65] B. C. Clark, L. J. Kerr, and S. Hama, Phys. Rev. C **67**, 054605 (2003).

[66] C. J. Batty, E. Friedman, H. J. Gils, and H. Rebel, Adv. Nucl. Phys. **19**, 1 (1989).

[67] E. W. Otten, in *Treatise on Heavy-Ion Science*, edited by D. A. Bromley (Plenum, New York, 1989), Vol. VIII, pp. 517–638.

[68] M. M. Sharma, G. A. Lalazissis, J. König, and P. Ring, Phys. Rev. Lett. **74**, 3744 (1995).

[69] N. Tajima, P. Bonche, H. Flocard, P.-H. Heenen, and M. S. Weiss, Nucl. Phys. **A551**, 434 (1993).

[70] R. R. Kinsey *et al.*, *The NUDAT/PCNUDAT Program for Nuclear Data* (1997), 9th International Symposium of Capture Gamma-Ray Spectroscopy and Related Topics, Budapest, Hungary, October 1996. Data extracted from the NUDAT database, version March 20, 1997, National Nuclear Data Center WorldWideWeb site.

[71] C. Legrand, E. Suraud, and P.-G. Reinhard, J. Phys. B **35**, 1115 (2002).

[72] M. Bender, W. Nazarewicz, and P.-G. Reinhard, Phys. Lett. **B515**, 42 (2001).

[73] J. P. Schiffer, S. J. Freeman, J. A. Caggiano, C. Deibel, A. Heinz, C.-L. Jiang, R. Lewis, A. Parikh, P. D. Parker, K. E. Rehm *et al.*, Phys. Rev. Lett. **92**, 162501 (2004).

[74] S. Bjørnholm and J. E. Lynn, Rev. Mod. Phys. **52**, 725 (1980).

[75] A. Mamdouh, J. M. Pearson, M. Rayet, and F. Tondeur, Nucl. Phys. **A644**, 389 (1998).

[76] S. Ćwiok, J. Dobaczewski, P.-H. Heenen, P. Magierski, and W. Nazarewicz, Nucl. Phys. **A611**, 211 (1996).

[77] M. Bender, K. Rutz, P.-G. Reinhard, J. A. Maruhn, and W. Greiner, Phys. Rev. C **58**, 2126 (1998).

[78] T. Bürvenich, K. Rutz, M. Bender, P.-G. Reinhard, J. A. Maruhn, and W. Greiner, Eur. Phys. J. A **3**, 139 (1998).

[79] T. Bürvenich, D. G. Madland, J. A. Maruhn, and P.-G. Reinhard, Phys. Rev. C **65**, 044308 (2002).

[80] A. Sobiczewski, Z. Patyk, and S. Ćwiok, Phys. Lett. **B224**, 1 (1989).

[81] M. Rufa, P.-G. Reinhard, J. A. Maruhn, W. Greiner, and M. R. Strayer, Phys. Rev. C **38**, 390 (1988).

[82] G. A. Lalazissis, J. König, and P. Ring, Phys. Rev. C **55**, 540 (1997).

[83] Yu. Ts. Oganessian *et al.*, Nature **400**, 242 (1999).

[84] Y. T. Oganessian *et al.*, Phys. Rev. C **62**, 041604(R) (2000).

[85] Y. T. Oganessian *et al.*, Phys. Rev. C **63**, 011301(R) (2000).

[86] M. Bender, K. Rutz, P.-G. Reinhard, J. A. Maruhn, and W. Greiner, Phys. Rev. C **60**, 034304 (1999).

[87] A. T. Kruppa, M. Bender, W. Nazarewicz, P.-G. Reinhard, T. Vertse, and S. Ćwiok, Phys. Rev. C **61**, 034313 (2000).

[88] J.-F. Berger, L. Bitaud, J. Decharge, M. Girod, and K. Dietrich, Nucl. Phys. **A685**, 1c (2001).

[89] T. Bürvenich, M. Bender, J. A. Maruhn, and P.-G. Reinhard, Phys. Rev. C **69**, 014307 (2004).

[90] M. Bender, K. Rutz, P.-G. Reinhard, and J. A. Maruhn, Eur. Phys. J. A **7**, 467 (2000).